Space-time mesh adaptation for solute transport in randomly heterogeneous porous media.

Aronne Dell'Oca[1], Giovanni Michele Porta[1], Alberto Guadagnini[1,2], Monica Riva[1,2]

[1]Dipartimento di Ingegneria Civile e Ambientale, Politecnico di Milano, Piazza L. Da Vinci 32, 20133 Milano, Italy

[2]Department of Hydrology and Atmospheric Sciences, University of Arizona, Tucson, AZ 85721, USA

Correspondence to: aronne.delloca@polimi.it

Keywords: adaptive discretization, solute transport, randomly heterogeneous media.

Abstract

We assess the impact of an anisotropic space and time grid adaptation technique on our ability to solve numerically solute transport in heterogeneous porous media. Heterogeneity is characterized in terms of the spatial distribution of hydraulic conductivity, whose natural logarithm, Y, is treated as a second-order stationary random process. We consider nonreactive transport of dissolved chemicals to be governed by an Advection Dispersion Equation at the continuum scale. The flow field, which provides the advective component of transport, is obtained through the numerical solution of Darcy's law. A suitable recovery-based error estimator is analyzed to guide the adaptive discretization. We investigate two diverse strategies guiding the (space-time) anisotropic mesh adaptation. These are respectively grounded on the definition of the guiding error estimator through the spatial gradients of: (*i*) the concentration field only; (*ii*) both concentration and velocity components. We test the approach for two-dimensional computational scenarios with moderate and high levels of heterogeneity, the latter being expressed in terms of the variance of Y. As quantities of interest, we key our analysis towards the time evolution of section-averaged and point-wise solute breakthrough curves, second centered spatial moment of concentration, and scalar dissipation rate. As a reference against which we test our results, we consider corresponding solutions associated with uniform space-time grids whose level of refinement is established through a detailed convergence study. We find a satisfactory comparison between results for the adaptive methodologies and such reference solutions, our adaptive technique being associated with a markedly reduced computational cost. Comparison of the two adaptive strategies tested suggests that: (*i*) defining the error estimator relying solely on concentration fields yields some advantages in grasping the key features of solute transport taking place within low velocity regions, where diffusion-dispersion mechanisms are dominant; and (*ii*) embedding the velocity field in the error estimator guiding strategy yields an improved characterization of the forward fringe of solute fronts which propagate through high velocity regions.

1 Introduction

A critical challenge to the characterization of solute transport in heterogeneous porous materials is the development of numerical methodologies rendering suitable approximations of the space-time dynamics of concentration fields in the presence of marked spatial contrasts of the medium hydraulic parameters, such as conductivity.

This study is focused on transport of non-reactive chemicals in heterogeneous porous media at the continuum scale, as described through the classical Advection Dispersion Equation (ADE). Effective dispersion coefficients appearing in the ADE accounts (in principle) for the enhancement of solute dispersion due to the unresolved velocity variability at scales which are not explicitly included in the model (see, e.g., Bijeljic and Blunt, 2006; Dentz and de Barros, 2015; de Barros and Dentz, 2016). This picture is consistent with the dispersion setting in capillary tubes (Taylor, 1953; Salles et al., 1993) where hydrodynamic dispersion arises from enhanced diffusion due to the presence of a spatial velocity distribution. The advection term appearing in the ADE accommodates the resolved details of the velocity field emerging from the solution of the flow problem. In the past two decades a considerable amount of literature focuses on the analysis of transport features which are not consistent with the ADE formulation (most notably, e.g., long tails of solute breakthrough curves, corresponding to long residence times of solute mass within the domain). These observations has substantiated the development of models which can capture non-Fickian (or so-called anomalous) transport features. These are based on approaches which include space-time non local theories (e.g., Cushman and Ginn, 1993; Guadagnini and Neuman, 2001; Morales-Casique et al., 2006a, b), continuous time random walk (CTRW, Berkowitz et al., 2006), fractional derivatives (Zhang et al., 2007) and multi-rate mass transfer concepts (Haggerty et al., 2004). All of these effective formulations include nonlocal transport terms, a framework relating all of them being presented by Neuman and Tartakovsky (2009).

According to a number of recent studies, the ability of the ADE-based mathematical formulation to interpret solute transport processes in randomly heterogeneous media is largely tied to the level of

descriptive detail associated with the characterization of the system properties. For example, results of Riva et al. (2008, 2010) suggest that apparent non-Fickian features observed in field-scale data are captured by the use of an ADE through an appropriate description of the (random) three-dimensional heterogeneity of the aquifer, and hence of the velocity field. In this context, the space-time resolution selected to approximate the ADE can have a considerable impact on the ability of the model to interpret observed results (e.g., Lawrence and Rubin, 2007). It is then relevant to be able to approximate the ADE with a sufficiently refined space-time resolution to retain the relevant details of the input heterogeneous conductivity (or trasmissivity) field, as the spatial organization of preferential pathways can imprint important transport features of transport (Edery et al., 2014). An *a priori* selection of the most suitable space and time discretization becomes then a challenging task. This aspect is exacerbated in highly heterogeneous media where solutes can typically travel relatively fast along preferential pathways and reside for long times in low-velocity regions.

A convenient way to design a mesh according to which the space-time domain is discretized is to rely on a setting characterized by a uniform numerical grid in space and a fixed time step across the simulation window. In this context, an appropriate discretization grid can be identified through a typical grid convergence analysis. The latter is based upon the solution of the numerical problem through diverse space / time discretization levels, obtained through a sequential uniform refinement of the spatial mesh and of the time step. This type of approach can lead to unaffordable computational costs as the domain size increases and/or a detailed description of the tracer plume is needed. Adaptive discretization techniques provide a valuable alternative. The basic idea of adaptive discretization is to exploit the features of the solution to increase or decrease automatically the space and time resolution associated with the numerical approximation. As a consequence, the element and time step size (and eventually the element shape) is not chosen *a priori*, but dynamically adjusted. This is typically obtained upon relying on a specific error indicator. A series of previous works provides examples of implementation of adaptive grids in the context of numerical modeling of flow (Knupp, 1996; Cao and Kitanidis, 1999; Cirpka et al., 1999; Mehl and Hill, 2002; Bresciani et al., 2012;

91 Jayasinghe, 2015) and solute transport scenarios in homogenous (see, e.g., Pepper and
92 Stephenson,1995; Kavetski et al., 2002; Saaltink et al., 2004; Younes and Ackerer, 2010) and
93 heterogeneous (see, e.g., Huang and Zhan, 2005; Klieber and Rivière, 2006; Chueh et al., 2010;
94 Gedeon and Mallants, 2012; Amaziane et al., 2014; Mansell et al., 2002 and references therein)
95 porous media. Amaziane et al. (2014) employ both space and time adaptive technique for simulating
96 radionuclide transport in block-wise heterogeneous media. In their approach, these authors did not
97 incorporate the anisotropic features of the solution to guide the spatial adaptation of the grid.
98 Jayasinghe (2015) implement an anisotropic spatial and temporal step refinement for single- and two-
99 phase flow taking place in a homogenous field scale scenario. An advantage of anisotropic mesh
100 adaptivity is that the size, orientation and shape of the elements are optimized to match the directional
101 features of the problem considered.
102 Our study is viewed in this context. A distinctive original aspect of our work is that we combine
103 anisotropic mesh and time step adaptation to simulate solute transport within randomly heterogeneous
104 media. We characterize heterogeneity of the considered porous systems in terms of the spatial
105 distribution of hydraulic conductivity, whose natural logarithm, Y, is treated as a second-order
106 stationary random process This conceptualization of the medium is at the basis of a large body of
107 works in the field of stochastic groundwater hydrology (see, e.g., Dagan, 1989 amongst others). By
108 performing a detailed study on single realizations of the conductivity field, our work provides an
109 assessment of the reliability of adaptive grid techniques to be employed within uncertainty
110 quantification and model calibration procedures.
111 Our works starts from the anisotropic mesh and time step adaptive discretization technique recently
112 proposed by Esfandiar et al. (2014, 2015). The latter relies on the *a posteriori* recovery-based error
113 estimators for space and time discretization errors presented by Micheletti and Perotto (2010) and
114 Porta et al. (2012a,b). Esfandiar et al. (2015) assess the impact of employing a space and time
115 adaptation procedure in the context of parameter estimation. They do so upon comparing parameter
116 estimates obtained through inverse modeling of solute transport within a laboratory-scale block-wise

heterogeneous flow cell. Their results show that implementation of the space-time adaptive methodology yields improved quality of parameter estimates as compared against those obtained using fixed uniform discretization characterized by a seemingly sufficient resolution.

Here, we extend the adaptive discretization technique of Esfandiar et al. (2015) and apply it to modeling solute transport in single realizations of randomly heterogeneous porous media. We follow the typical procedure of solving the flow problem on a fixed numerical grid. The latter is designed to honor the spatial structure of the random conductivity field. The resulting velocity field may exhibit a complex spatial arrangement, including the occurrence of high velocity regions where flow is channeled and large stagnant zones that may originate non-Fickian solute transport features displayed by spatially averaged solute breakthrough curves (Edery et al., 2014). Spatial dynamic adaptation entails performing coarsening and refinement of the computational mesh/grid at each time step. In this context, a critical challenge to an effective implementation of dynamically adaptive spatial meshes is the requirement of projecting the velocity field onto the adapted mesh. The latter could be characterized by local element sizes which may be unrelated to the original mesh employed to characterize flow across the hydraulic conductivity field.

Here, we investigate two diverse strategies guiding the anisotropic meshes adaptation. The error estimator associated with each of these strategies is assessed on the basis of spatial gradients of (*i*) solute concentration only, or (*ii*) both concentration and fluid velocity components. With reference to the latter implementation, we follow the procedure proposed by Porta et al. (2012a) to combine diverse error indicators to drive mesh adaptation. Embedding the velocity components in the error estimator is an original feature of our study and is consistent with the feedback between the spatial derivatives of the components of the velocity vector and the observed folding, stretching, mixing and spreading of the evolving concentration plume. The latter have emerged as remarkable features, which are particularly evident in highly heterogeneous media (see, e.g., Le Borgne et al., 2015).

To assess the quality of the adaptive methodologies implemented, we focus on the temporal evolution of both local and spatially integrated concentrations as well as global spreading and mixing indicators. These include the second centered spatial moment of concentration and the scalar dissipation rate.

The rest of the study is organized as follows. Section 2 describes the problem setting, Section 3 being devoted to a brief recounting of the main features of the adaptive methodology of Esfandair et al. (2014, 2015). Results and comparisons of the adaptive space-time discretization techniques are illustrated in Section 4. Conclusions are drawn in Section 5.

2 Problem Setting

2.1 Mathematical and Numerical Model

We consider a two-dimensional rectangular domain, Ω, of height $H = 0.14\ m$ and width $L = 0.04\ m$. We denote the horizontal and the vertical direction with y, z, respectively (see Fig. 1). The Advection Dispersion Equation (ADE) reads

$$\frac{\partial C}{\partial t} + \boldsymbol{v} \cdot \nabla C - \nabla \cdot \left(\boldsymbol{D} C \right) = 0 , \tag{1}$$

where $C = C(\boldsymbol{x}, t)$ [-] is solute concentration at location $\boldsymbol{x}$ and time t, $\boldsymbol{v}$ [LT^{-1}] is the velocity vector (v_y and v_z respectively denote horizontal and vertical velocity components), and $\boldsymbol{D}$ [L^2T^{-1}] is the local dispersion tensor given by

$$\boldsymbol{D} = \left(\alpha_T + D_m \right) \delta_{ij} + \left(\alpha_L - \alpha_T \right) \frac{v_i v_j}{|\boldsymbol{v}|} \quad \text{with} \quad i, j = y, z . \tag{2}$$

Here, α_T [L] and α_L [L] respectively are transverse and longitudinal dispersivity; D_m [L^2T^{-1}] is molecular diffusion; δ_{ij} is the Kronecker' delta; and $|\boldsymbol{v}|$ is the velocity modulus. We set $\alpha_T = \alpha_L = \alpha = 10^{-3} m$ and $D_m = 10^{-9} m^2 / s$ in our showcase examples. The imposed boundary conditions for Eq.s (1)-(2) are (see also Fig. 1c) as follows: a time-varying concentration C_{BC} is set along the bottom edge of the domain, according to $C_{BC} = e^{3-t}$; impermeable boundary conditions are prescribed along the vertical edges; and a free boundary condition is imposed at the top of the domain,

i.e., $\nabla C \cdot \mathbf{n} = 0$, $\mathbf{n}$ being the normal unit vector to the boundary (see also Fig. 1a). Solute concentration is zero everywhere in the domain at the initial simulation time.

We consider a steady-state advective velocity field, $\boldsymbol{v}$, whose spatial structure is driven by the typical formulations

$$\nabla \cdot \boldsymbol{v} = 0 \ , \qquad \boldsymbol{v} = -\frac{K}{\phi} \nabla h , \tag{3}$$

where h [L] is hydraulic head, and ϕ [-] is porosity, which we take as uniform and set as ϕ = 0.35. The imposed boundary conditions for Eq. (3) are (see also Fig. 1b): fixed head along the bottom edge, h_{BC}; no-flow along the vertical edges; and imposed constant vertical velocity, $v_{z,BC} = 7.0 \times 10^{-3} m/s$, at the top boundary. The hydraulic conductivity of the porous medium is modeled as an isotropic random field $K = K_G e^{Y(y,z)}$ [LT^{-1}], $K_G = 10^{-9} m/s$ being the geometric mean of K and Y a zero-mean second-order stationary random process characterized by the isotropic exponential covariance function

$$C_Y = \sigma_Y^2 \, e^{-\frac{|\mathbf{r}|}{l}} . \tag{4}$$

Here, $\mathbf{r}$, σ_Y^2, l respectively are the separation vector (or lag) between two points in space, variance and correlation length of Y. In our examples, we set l = 0.02 m, corresponding to H/l = 7 and L/l = 2. We consider a mildly (σ_Y^2 = 1) and a strongly (σ_Y^2 = 5) heterogeneous Y field, to explore the effects of increasing level of complexity of the velocity and concentration distributions on the grid adaptation strategy. The heterogeneous conductivity fields are synthetically generated by the widely used and tested code SGSIM (Deutsch and Journel, 1998) on a uniform grid with $n_y = 50$ and $n_z = 175$ elements, respectively along the y and z directions. Note that this corresponds to characterize the conductivity field through 25 generation points per correlation length, which ensures attaining a high level of descriptive detail of the heterogeneity in K. Hereinafter we label as ΔK the size of the square

element of the uniform mesh employed for generating *K*. Fig. 1a depicts the realization of *Y* employed for the test case with $\sigma_Y^2 = 5$.

Transport simulations are performed across a time window of length $T = 4t_{PV}$ and $T = 2t_{PV}$, respectively for $\sigma_Y^2 = 5$ and $\sigma_Y^2 = 1$, $t_{PV} = H / v_{z,BC} = 200\ s$ corresponding to a pore volume. A global Péclet number $Pe = lv_{z,BC} / \left(D_m + v_{z,BC}\alpha\right)$ can be defined as the ratio between average diffusion-dispersion and advective time scales. In our numerical test cases $Pe = 20.0$.

Following Esfandiar et al. (2014, 2015), we discretize Eq.s (1)-(2) by means of a stabilized finite element method, which is based on a streamline diffusion technique (Brooks and Hughes, 1991). Spatial discretization is performed upon relying on a spatial mesh $\mathfrak{T}_h = \{E\}$, which results in a conformal discretization of Ω into triangular elements *E*. Discretization of the time window [0, *T*] is performed upon introducing the time levels $\{t^0 = 0, .., t^n = T\}$, which define the set $\{I_k\}$ of the time intervals I_k of amplitude $\Delta t^k = t^{k+1} - t^k$. Time discretization is performed through the standard θ-method (Quarteroni et al., 2007). We resort to an implicit scheme and set θ= 2/3 to guarantee the unconditionally absolute stability of the θ -method. The numerical solution of the flow problem in Eq. (3) relies on a standard finite element of degree two for the pressure. As such, velocity components are obtained as piecewise linear functions through Eq. (3).

Fig. 1b depicts the resulting spatial distribution of the natural logarithm of the modulus of $\boldsymbol{v}$, $\log\left(|\boldsymbol{v}|\right)$, for $\sigma_Y^2 = 5$. Note the complexity of the structure of the velocity field, as evidenced by the presence of a clearly defined low-velocity region and two preferential pathways characterized by large velocities (identified by black dashed curves in Fig. 1b). Fig. 1c depicts the concentration field at *t* = 0.5 t_{PV} calculated on the same uniform mesh for $\sigma_Y^2 = 5$ (see details in Section 2.3).

2.2 Observables

We introduce here the quantities which constitute the key target outputs for the purpose of our analyses. We consider the temporal variation of solute concentration at given locations within the computational domain, i.e.,

$$C_F(t) = C(y_F, z_F, t) \qquad C_S(t) = C(y_S, z_S, t) \tag{5}$$

where $P_F = (y_F, z_F)$ and $P_S = (y_S, z_S)$ indicate the locations in the domain where $|\boldsymbol{v}|$ is largest and lowest, respectively (i.e., subscripts *F* and *S* respectively correspond to fast and slow regions). We find ($y_F = 3.8\times10^{-2} m$; $z_F = 3.8\times10^{-2} m$) and ($y_S = 1.5\times10^{-2} m$; $z_S = 3.6\times10^{-2} m$) for the highly heterogeneous test case ($\sigma_Y^2 = 5$), as depicted in Fig. 1c. Otherwise, we obtain ($y_F = 4\times10^{-3} m$; $z_F = 6.9\times10^{-2} m$) and ($y_S = 1.8\times10^{-2} m$; $z_S = 3.3\times10^{-2} m$) for the field with $\sigma_Y^2 = 1$.

We also consider section-averaged concentrations, mimicking typically observed breakthrough curves, i.e.,

$$\overline{C}_i = \frac{1}{L}\int_L C(y, z_i, t)dy \qquad \text{with} \qquad i \in \{1,2,3\}, \tag{6}$$

where $\overline{C}_1$ is evaluated at $z_1 = H/4$, $\overline{C}_2$ at $z_2 = H/2$, and $\overline{C}_3$ at $z_3 = H$ (see Fig. 1c).

We then focus on globally integrated quantities, which can quantify spreading and mixing of the plume within the domain. To this end, we consider the second centred spatial moment of the concentration plume along the *z*-direction, which has a relevant role for the characterization of solute plume spreading and is defined as

$$S_{zz}(t) = \frac{1}{M(t)\Omega}\int_\Omega \left[z - z_{AV}(t)\right]^2 C(\boldsymbol{x}, t)d\Omega \qquad \text{with} \qquad M(t) = \int_\Omega C(\boldsymbol{x}, t)\, d\Omega, \tag{7}$$

where z_{AV} is the center of mass of the plume at time *t*, i.e.,

$$z_{AV}(t) = \frac{1}{M(t)\Omega}\int_\Omega z\, C(\boldsymbol{x}, t)d\Omega. \tag{8}$$

We finally consider the scalar dissipation rate

$$\chi(t) = \int_{\Omega} \nabla C^T \boldsymbol{D} \nabla C d\Omega \tag{9}$$

which quantifies the rate of mixing of the plume and is markedly important for the study of mixing-driven reactive transport (see, e.g., De Simoni et al., 2005, and references therein).

2.3 Fixed Uniform Discretization

We solve flow (Eq. (3)) and transport (Eq. (1)) in the set-up described in Section 2.1 for a series of fixed uniform triangular meshes, each associated with an increased level of spatial discretization and decreased width of the time step. Increasing levels of space-time refinement are analyzed until convergence of the numerical results is attained. As a convergence criterion, we impose that all of the integrated quantities of interest (Eq.s (6)-(9)) do not exhibit a relative absolute error larger than 1% and that the pointwise breakthrough curves (see Eq. (5)) do not exhibit a relative absolute error larger than 5% between two consecutive levels of refinement. As a starting grid, corresponding to a first level of discretization, we select a structured Cartesian grid where the distances Δy and Δz between two nodes along the *y* and *z* axes coincide with ΔK. The resulting mesh, here termed *G*1, is formed by $n_{G1} = 17,500$ triangles. As a second level of discretization (corresponding to mesh *G*2), we subdivide each conductivity element into four sub-elements, each of which is composed of two triangles. In this configuration, the length of the edges of the triangles are $\Delta y = \Delta z = \Delta K / 2$ and *G*2 comprises $n_{G2} = 70,000$ elements. We proceed according to this strategy until we reach a level of refinement corresponding to $\Delta y = \Delta z = \Delta K / 6$ for mesh *G*6. The latter is then composed of $n_{G6} = 630,000$ triangles. With reference to the time step, we analyze three different values, i.e., $\Delta t_1 = 10^{-1} s$, $\Delta t_2 = 5 \times 10^{-2} s$ and $\Delta t_3 = 2.5 \times 10^{-2} s$. Our results indicate that the quantities of interest introduced in Section 2.2 attain convergence at *G*5 (formed by $n_{G5} = 437500$ triangles) and for $\Delta t_2 = 5 \times 10^{-2} s$. In the following, the results associated with *G*6 and $\Delta t_2 = 5 \times 10^{-2} s$ represent our reference solution for the fixed time-space discretization and results for the adaptive procedure will be compared against these.

3 Adaptive Discretization Technique

We briefly recall here the main features of the adaptive discretization methodology. The latter has been previously applied to shallow water modeling (Porta et al., 2012b) and computational fluid dynamics (Micheletti et al., 2010) settings. Esfandiar et al. (2015) applied this procedure to analyze solute transport within homogeneous and block-wise heterogeneous porous media.

The adaptive technique is grounded on the definition of an *a posteriori* error estimator for the global (space-time) discretization error

$$\eta_{ht}^{A} = \eta_{h}^{A} + \eta_{t} \,, \tag{10}$$

where η_h^A is an anisotropic spatial error estimator that enables us to optimize the size, shape, orientation of the mesh elements and η_t is an error estimator for the time discretization. We compute the two terms in Eq. (10) by relying on recovery-based error estimators (Zienkiewicz and Zhu, 1987), in the form introduced by Micheletti and Perotto (2010) and Porta et al. (2012b).

3.1 Anisotropic Mesh Adaptation

Let C_h be the piece-wise linear finite element approximation of concentration in the solution of Eq. (1), which is defined on mesh $\mathcal{T}_h$. We follow Porta et al. (2012a) and Micheletti and Perotto (2010) and introduce the local anisotropic estimator

$$\left[\eta_{E,C}^{A}(t)\right]^2 = \frac{1}{\lambda_{1,E}\lambda_{2,E}} \int_{\Delta E} \left\{ \lambda_{1,E}^2 \left[\mathbf{r}_{1,E} \cdot \left(P_R\left(C_h(t)\right) - \nabla C_h(t) \right) \right]^2 + \lambda_{2,E}^2 \left[\mathbf{r}_{2,E} \cdot \left(P_R\left(C_h(t)\right) - \nabla C_h(t) \right) \right]^2 \right\} d\Delta E \quad E \in \mathcal{T}_h, \;\; t > 0 \,. \tag{11}$$

Here, $\lambda_{i,E}$ and $\mathbf{r}_{i,E}$ (i = 1, 2) respectively identify the eigenvalues and the eigenvectors of the tensor $\mathbf{M}_E$, defining the mapping between a reference triangle $\hat{E}$ and the generic element E of $\mathcal{T}_h$ (see Fig. 2a). Note that $\lambda_{i,E}$ are measures of the length of the semi-axes of the ellipse circumscribing E, while $\mathbf{r}_{i,E}$ identify the directions of these semi-axes (Formaggia and Perotto, 2001, 2003). The quantity $P_R\left(C_h(t)\right)$ represents the recovered spatial gradient of C_h at time t. As depicted in Fig. 2b, $P_R\left(C_h\right)$

is computed as the area-weighted average of the discrete gradient $\nabla C_h(t)$ within the patch ΔE of triangles sharing at least one vertex with *E*. The *a posteriori* estimator of the global error associated with the finite element spatial discretization of the concentration field is computed as

$$\left[\eta_C^A(t)\right]^2 = \sum_{E\in\mathbb{T}_h}\left[\eta_{E,C}^A(t)\right]^2 \qquad t>0. \tag{12}$$

Eq. (12) represents an anisotropic error estimate, because it directly involves the anisotropic quantities $\lambda_{i,E}$ and $\mathbf{r}_{i,E}$ identifying the size, shape, and orientation of element *E*. We refer to Porta et al. (2012a, b) and Micheletti and Perotto (2010) for a rigorous illustration of the error estimator in Eq.s (11)-(12) and its application. This adaptation strategy and the associated results will be referred to as $G_{\nabla C}$ in the following.

Together with Eq. (12), we consider in this work an additional version of the error estimator. The latter is constructed with the aim of embedding the spatial variability of the velocity components. Let us then assume that the field $\tilde{\boldsymbol{v}}_h = (u_h, \tilde{v}_h)$ represents the piece-wise linear interpolation of the velocity field on the adapted mesh $\mathbb{T}_h$. We introduce the dimensionless components

$$U_h = \frac{u_h - \min(u_h)}{\max(u_h) - \min(u_h)}, \qquad V_h = \frac{\tilde{v}_h - \min(\tilde{v}_h)}{\max(\tilde{v}_h) - \min(\tilde{v}_h)}, \tag{13}$$

which we embed in the following definition for the error estimator

$$\left[\eta_{E,U}^A(t)\right]^2 = \begin{cases} 0, \ if\ C_{h,E}(t) < 10^{-7} \\ \dfrac{1}{\lambda_{1,E}\lambda_{2,E}}\displaystyle\int_{\Delta E}\Big\{\lambda_{1,E}^2\left[\mathbf{r}_{1,E}\cdot\left(P_R(U_h)-\nabla U_h\right)\right]^2 \\ \qquad +\lambda_{2,E}^2\left[\mathbf{r}_{2,E}\cdot\left(P_R(U_h)-\nabla U_h\right)\right]^2\Big\}d\Delta E, \ if\ C_{h,E}(t)\geq 10^{-7} \end{cases} \tag{14}$$

Here, $C_{h,E}(t)$ represents the average concentration in the mesh triangle *E* at time *t*. We can also define an error estimator $\eta_{E,V}^A(t)$ upon replacing U_h with V_h in Eq. (14). It is then possible to use Eq. (14) to obtain global error estimates η_U^A and η_V^A in the form of Eq. (12). Note that the error estimator in Eq. (14) is defined as a measure of the variability of the dimensionless velocity component U_h, and is also

conditional to the value of local concentration $C_{h,E}(t)$. This choice is consistent with our aim, which is directed towards targeting grid refinement across portions of the domain where solute mass is present, i.e., where transport phenomena are active at a given time.

We aim here at embedding in a unique error indicator the information on the spatial distribution of concentration and on the velocity components. Following Porta et al. (2012b), we then define a global error estimator

$$\left[\eta^A_{CUV}(t)\right]^2 = \frac{1}{3}\left(\left[\eta^A_C(t)\right]^2 + \left[\eta^A_U(t)\right]^2 + \left[\eta^A_V(t)\right]^2\right) \tag{15}$$

where the concentration field and the velocity components are jointly employed to guide the grid adaptive procedure. This adaptation strategy and the associated results will be referred to as $G_{\nabla CUV}$ in the following. Note that an error estimator in which different quantities are combined has been previously employed in Porta et al. (2012a) in the context of shallow water equations. Here, we apply the same concept to the numerical solution of Eq. (1), where the velocity components are parameters (and not unknowns) of the problem. We do so on the basis of the observation that the solution of Eq. (1) requires projecting the velocity components onto the grid employed to compute concentration. We use a linear interpolation of the velocity field between the mesh employed to solve Eq. (3) and the mesh where C_h is computed. The indicator in Eq. (15) is designed to control the error associated with the solution of C_h as well as the one related to the interpolation of U_h, V_h.

The final goal of our procedure is to construct an anisotropic spatial mesh driven by the estimator in Eq. (12) or Eq. (15). Let us assume here that C_h, U_h, V_h are known piece-wise linear functions on a generic grid $\mathfrak{T}_h$. Our aim is then to generate a new mesh, which is designed to minimize the selected error, conditional to a given number of mesh elements. For the purpose of our demonstration, we set the number of elements of the adapted grid to $N_{ele} \approx 10^4$. The mesh adaptation procedure can be summarized as follows:

1. We set a global tolerance τ and impose that the same error τ_E is assigned to each triangle E of $\mathcal{T}_h$; this criterion is typically denoted as the error equidistribution principle (Formaggia and Perotto, 2003).
2. We solve a constrained local optimization problem in each triangle E of the mesh yielding the optimal values of $\lambda_{i,E}^{new}$ and $\mathbf{r}_{i,E}^{new}$ ($i = 1, 2$) for all triangles in the mesh $\mathcal{T}_h$ (see, e.g., Formaggia and Perotto, 2003). This allows computing a metric tensor field $\mathbf{M}_{E,0}^{new}$.
3. We aim at adapting a mesh such that the number of elements (i.e., the mesh cardinality) is fixed *a priori*. To this end, we apply a global and uniform rescaling of the metric tensor field $\mathbf{M}_{E,0}^{new}$ to obtain a new tensor field $\mathbf{M}_{E}^{new}$, which is associated with the desired number of elements. Note that the rescaling of the metric field relies on an *a priori* estimation of the area of the elements, which can be obtained from the optimized quantities $\lambda_{i,E}^{new}$ and $\mathbf{r}_{i,E}^{new}$, i.e., it does not require to iteratively generate the mesh $\mathcal{T}_h^{new}$.
4. Once $\mathbf{M}_{E}^{new}$ is known, we generate the adapted mesh $\mathcal{T}_h^{new}$ through the metric-based mesh generator BAMG (Hecht, 2012).

Some constraints are imposed to the mesh adaptation procedure to guarantee the robustness of the methodology. Excessive element clustering is locally prevented by setting a minimum threshold value ($p_{\min} = 10^{-9}$ in our test cases) for the product $\lambda_{1,E}^{new}\lambda_{2,E}^{new}$ within the local optimization solution. This is tantamount to assigning a lower limit on the element area, because $|E| = |\hat{E}|\lambda_{1,E}\lambda_{2,E}$. In this work we do not impose any constraint on the maximum size of grid elements. Note that it would be possible to control the maximum size of an element, e.g., by imposing an upper bound to the product $\lambda_{1,E}^{new}\lambda_{2,E}^{new}$.

3.2 Time Step Adaptation

Time step adaptation is implemented upon relying on a recovery-based estimate of the time discretization error. We aim at predicting the time step Δt^k that can be used at each time level t^k for the subsequent advancement in time. The recovery-based estimator for the time discretization error within time interval $I_{k-1} = \left[t^{k-1}, t^k \right]$ is then defined as (Porta et al., 2012b)

$$\left[\eta^t_{I_{k-1}} \left(\boldsymbol{x} \right) \right]^2 = \Delta t^{k-1} \int_{I_{k-1}} \left| \frac{\partial C_R \left(\boldsymbol{x} \right)}{\partial t} |_{I_{k-1}} - \frac{C^k_h \left(\boldsymbol{x} \right) - C^{k-1}_h \left(\boldsymbol{x} \right)}{\Delta t^{k-1}} \right|^2 dt \tag{16}$$

where $C_R \left(\boldsymbol{x} \right)$ is a recovered solution, coinciding with the parabola which interpolates the concentration values $\left[C^{k-2}_h \left(\boldsymbol{x} \right), C^{k-1}_h \left(\boldsymbol{x} \right), C^k_h \left(\boldsymbol{x} \right) \right]$ at times $\left[t^{k-2}, t^{k-1}, t^k \right]$, respectively (see Fig. 3a); and $C^k_h \left(\boldsymbol{x} \right)$ is the numerically computed concentration at time t^k and at point $\boldsymbol{x}$. Note that the multiplicative factor Δt^{k-1} in Eq. (16) renders the time error estimator dimensionless, consistent with the spatial error estimator in Eq. (12) and Eq. (15). In this work, the estimator in Eq. (16) is always evaluated on the basis of the concentration C_h, because flow is steady-state and the fluid velocities are then constant in time (even if variable in space). The recovery-based error estimator in Eq. (16) is evaluated at each *i*-node, i.e., N_i, of the current mesh $\mathbb{T}_h$. The time error estimator over the whole space domain is obtained as an area weighted average

$$\left[\eta^t_{I_{k-1}} \right]^2 = \left[\Delta t^{k-1} \rho^t_{I_{k-1}} \right]^2 . \tag{17}$$

with

$$\left[\rho^t_{I_{k-1}} \right]^2 = \frac{\sum_{E \in \mathbb{T}_h} \left(1/3 \sum_{N_i \in E} \left[\eta^t_{I_{k-1}} \left(N_i \right) \right]^2 \right)^2 |E|}{\left[\Delta t^{k-1} \right]^2 \sum_{N \in \mathbb{T}_h} |E|} \tag{18}$$

The new time step is computed by (a) substituting in (17) Δt^{k-1} with Δt^k in order to obtain a time error estimator associated with interval I_k, i.e. $\eta^t_{I_k}$; (b) imposing a tolerance for time error estimator, $\eta^t_{I_k} = \tau^{\Delta t}_t = 10^{-6}$. As a result we obtain (Porta et al., 2012b; and Esfandiar et al., 2014)

$$\Delta t^k = \frac{\tau_t^{\Delta t}}{\eta_{I_{k-1}}^t} \Delta t^{k-1} \tag{19}$$

The predicted time step in Eq. (19) is constrained by a minimum and a maximum value. These are respectively set to $\Delta t_{MIN} = 0.05s$ (which coincides with the value selected for the uniform grid *G*6) and $\Delta t_{MAX} = 30s$ (which is chosen to avoid excessive coarsening of the time discretization).

3.3 Solution adaptation procedure

We detail here all the steps we follow to obtain the numerical solution of Eq. (1) through our adaptive strategy. As a first step, we compute a reference velocity field by solving the flow problem in Eq. (3) on a fixed uniform and sufficiently fine grid $\mathbb{T}_h^F$. This enables us to obtain the numerical approximation of the fluid velocity field $\boldsymbol{v}_h\left(\mathbb{T}_h^F\right) = \left(u_h\left(\mathbb{T}_h^F\right), v_h\left(\mathbb{T}_h^F\right)\right)$. In this study we set $\mathbb{T}_h^F = G3$ to achieve a good balance between accuracy and computational costs.

We then illustrate in the following the way we employ the space-time adaptive procedure for a generic time level t^k. We do so by assuming the concentration $C_h^k = C_h(t^k)$ and the grid $\mathbb{T}_h^k$ to be known. The adaptive solution is employed to compute C_h^{k+1}, the adapted grid $\mathbb{T}_h^{k+1}$ and the new time level t^{k+1}. These are obtained through the following steps:

1. Obtain the velocity field $\tilde{\boldsymbol{v}}_h = \tilde{\boldsymbol{v}}_h\left(\mathbb{T}_h^k\right)$ upon projecting $\boldsymbol{v}_h\left(\mathbb{T}_h^F\right) = \left(u_h\left(\mathbb{T}_h^F\right), v_h\left(\mathbb{T}_h^F\right)\right)$ onto the grid $\mathbb{T}_h^k$. This is here performed through linear interpolation.
2. Solve the transport scenario, as described in Eq. (1), by employing the velocity field $\tilde{\boldsymbol{v}}_h = \tilde{\boldsymbol{v}}_h\left(\mathbb{T}_h^k\right)$ to determine the advective and dispersive parameters. This allows obtaining $C_h^{k+1}\left(\mathbb{T}_h^k\right)$.
3. Apply the mesh adaptation procedure relying on estimator in Eq. (12) or Eq. (15) and compute $\mathbb{T}_h^{k+1}$. As detailed in Section 3.2, we obtain this adapted grid so that the number of elements of $\mathbb{T}_h^{k+1}$ is approximately equal to 10^4.

4. Project the concentration fields $C_h^{k-1}, C_h^k, C_h^{k+1}$ onto the new grid $\mathcal{T}_h^{k+1}$ to obtain the adapted time step Δt^k. The next time level for the simulation is then defined as $t^{k+1} = t^k + \Delta t^k$.

The procedure is then repeated until $t^{k+1} \geq T$. Note that step 4 of the above procedure can be performed only when $k > 1$, i.e., the two steps $\Delta t^0, \Delta t^1$ are associated with a fixed time step Δt_{MIN}, which is assigned *a priori*, as anticipated in Section 3.2.

4 Results

We illustrate here the comparison of numerical results associated with the observables described in Section 2.2 and obtained relying on: (*a*) space-time adaptive methodology guided by error estimators based on the concentration fields only, i.e., Eq. (12), or the joint use of the concentration and velocity fields, i.e., Eq. (15); and (*b*) fixed time step and fixed uniform spatial discretization. In the latter case, we focus in the following on results obtained with a fixed discretization time interval set to Δt_2 and grids *G*6 and *G*1, respectively corresponding to the reference solution, and to a uniform grid characterized by a number of elements of the same order of magnitude as the two adaptive methodologies considered. We discuss results obtained for the highly heterogeneous field ($\sigma_Y^2 = 5$) in Section 4.1, and those obtained for mild heterogeneity ($\sigma_Y^2 = 1$) in Section 4.2.

4.1 Highly heterogeneous domain ($\sigma_Y^2 = 5$)

The selected realization of the log-conductivity field is depicted in Fig. 1a. Fig. 1b depicts the natural logarithm of the velocity modulus, i.e. $\log(|\boldsymbol{v}|)$, as obtained from the numerical discretization of the flow problem on the fixed uniform grid *G*3. As noted in Section 2.1, Fig. 1b reveals the presence of two high velocity channels (see dashed curves in Fig. 1b), which act as preferential pathways for fluid flow and are expected to drive transport behavior. An approximately circular low velocity region centered around location *z* = 0.035 m, *y* = 0.02 m is also identified (see dash-dotted circle in Fig. 1b). Fig. 1c depicts the resulting concentration field at $t = 0.5\ t_{PV}$. As a general observation, one can note

405 that solute mass distribution across the domain is largely influenced by the structure of the velocity
406 field, part of the mass being delayed due to the presence of the above mentioned low velocity region.
407 We start our analysis by focusing on the early-time features of the adapted mesh and resulting
408 concentration fields when applying adaption strategies $G_{\nabla CUV}$ and $G_{\nabla C}$. We compare the ensuing
409 results against those obtained by the reference solution. Fig. 4 depicts the concentration field obtained
410 at $t = 0.05\ t_{PV}$ by the three discretization strategies (Fig. 4a-c) and the adapted meshes (Fig. 4d-e). We
411 present concentrations in logarithmic scale, because small concentration values are critical to evaluate
412 early arrivals and tailing, which are often of interest in practical applications. All panels of Fig. 4 are
413 focused on a limited region located in the proximity of the inflow boundary. Analysis of Fig. 4a-c
414 shows that $G_{\nabla CUV}$ and $G_{\nabla C}$ yield a solution which is consistent with *G*6. We note that two solute
415 fingers appear at early times. This is due to the channeling in the velocity field around the low velocity
416 region zone highlighted in Fig. 1b.
417 The analysis of the spatial topology of the adapted grid $G_{\nabla C}$ reveals that the element size is relatively
418 coarse in the proximity of the forward solute fringe (see Fig. 4d). This can be seen, e.g., in the region
419 $y = [0, 0.01]\ m \times z = [0.04, 0.05]\ m$ and is consistent with the observation that concentrations vary
420 between approximately 10^{-7} and 10^{-4} in this region, i.e., the concentration gradient is lower than that
421 associated with other portions of the domain (see Fig. 4b). As a consequence, the log-concentration
422 field rendered by $G_{\nabla C}$ appears to be characterized by a local loss of accuracy. We also observe that
423 some oscillations (of the order of 10^{-6}-10^{-5}) appear in the solution. This is evident, for example, around
424 location ($y \approx 0.02$ m, $z \approx 0.02$ m). The emergence of these oscillations might be linked to the
425 interpolation of the solution between adapted meshes, which is in turn associated with some errors in
426 the presence of relatively coarse elements. The adapted mesh $G_{\nabla CUV}$ is characterized by elements of
427 small size all along the forward solute fringe. This is related to the observation that adaptation is also
428 guided by the spatial gradients of U_h and V_h, which are embedded in Eq.s (14)-(15). As a result, the
429 solution rendered by $G_{\nabla CUV}$ is capable of reproducing the fine scale details of the reference log-

concentration field, which are partially lost in $G_{\nabla C}$. We also observe that the shape of the triangular elements is nearly isotropic when the velocity components are considered for mesh adaptation, consistent with the isotropic correlation model selected for the spatial covariance of conductivity.

Fig. 5 depicts the log-concentration field for time $t = 1.5\ t_{PV}$, as given by (*a*) *G*6, (*b*) $G_{\nabla C}$, and (*c*) $G_{\nabla CUV}$. From a preliminary visual inspection, the concentration field displays smooth variations and the three solutions appear to be very similar. Solute mass remains trapped in the low velocity region located in the bottom part of the domain (see also Fig. 1b), solute being almost uniformly distributed across the system for $z > 0.07$ m. These features of the solution are reflected in the adapted meshes. Grid $G_{\nabla C}$ is refined within the low conductivity zone where relatively high concentration gradients arise (see Fig. 5d). Mesh $G_{\nabla CUV}$ is formed by elements of comparable size throughout a vast portion of the domain, i.e., at all locations where $C > 10^{-7}$ (see Fig. 5c and Fig. 5e). At these late times, visual inspection of the results indicates that the solutions obtained for *G*6, $G_{\nabla C}$ and $G_{\nabla CUV}$ share some similarities, even as the adapted meshes display marked differences. Fig. 6 depicts a magnification of the log-concentration field and of the adapted grids around the low velocity area at $t = 1.5\ t_{PV}$. The solution associated with mesh $G_{\nabla C}$ exhibits local variations of the order of 10^{-6}-10^{-5}. These are particularly evident at $z \approx 0.015$ m, i.e., the light blue fringes of log*C* observed in Fig. 6b do not appear in the reference solution (Fig. 6a) and when $G_{\nabla CUV}$ is considered (Fig. 6c). As previously noted, this result can be linked to local differences of the element size of the grids associated with $G_{\nabla C}$ and $G_{\nabla CUV}$. We observe that $G_{\nabla CUV}$ is composed of elements of mostly uniform size. Only mild variations in the element shape and orientation are detected in Fig. 6e and Fig. 5e. This implies that the footprint of the concentration field on the mesh topology is barely effective. Otherwise, the mesh $G_{\nabla C}$ is completely tied to the concentration field gradients and displays marked variations of the element size and shape around the low velocity area.

453 The evolution of the time step, Δt, as a function of time is depicted in Fig. 7 for $G_{\nabla CUV}$ (red curve)
454 and $G_{\nabla C}$ (blue curve). The lowest (Δt_{MIN}) and largest (Δt_{MAX}) allowed time step are also reported
455 in Fig. 7. The time steps at early times practically coincide with Δt_{MIN}, due to the rapid temporal
456 variation of the concentration field. As time advances, values of Δt larger than Δt_{MIN} are allowed.
457 This is so because the solute plume spreads over an increased portion of the domain and
458 diffusive/dispersive process gain importance leading to a reduced time variation of the concentration
459 fields. The combination of the time step and mesh adaptivity yields a relative speed up of the
460 computational costs. The ratio of the CPU time required by $G_{\nabla CUV}$ and *G*6, $CPU_{\nabla CUV/G6}$, and by $G_{\nabla C}$
461 and *G*6, $CPU_{\nabla C/G6}$, is respectively equal to $CPU_{\nabla CUV/G6} = 1.27 \times 10^{-1}$ and $CPU_{\nabla C/G6} = 1.56 \times 10^{-1}$.
462 We now proceed to analyze the behavior of the selected quantities of interest described in Section
463 2.2. Fig. 8a depicts the section-averaged concentrations $\overline{C}_i(t)$, with *i* = 1, 2, 3, evaluated for *G*6 (see
464 Fig. 1c). Asymmetry is a recurring feature of all $\overline{C}_i$ results. This behavior is linked to the level of
465 heterogeneity of the conductivity field (see, e.g., Riva et al., 2008, 2010; Edery et al., 2015). A marked
466 tailing behavior appears at late times. This is particularly evident in $\overline{C}_1$, due to the presence of the
467 low velocity region where solute accumulates at early times and from which it is subsequently slowly
468 released by diffusion-dispersion. For the sake of clarity, the comparison between the results obtained
469 with the strategies considered is then highlighted across a set of subpanels, each focusing on specific
470 parts of the $\overline{C}_i(t)$ curves. Fig. 8b depicts details of the early times behavior of $\overline{C}_1$ for *G*6 (black
471 curve), *G*1 (green curve), $G_{\nabla C}$ (blue curve) and $G_{\nabla CUV}$ (red curve). Overall, we observe that the
472 differences between section-averaged concentrations rendered by the various solutions are relatively
473 small (of the order of 10^{-5}). This can be also seen for intermediate and late solute arrivals, respectively
474 in Fig.s 8c and 8d. We observe that the fixed mesh *G*1 tends to underestimate the section-averaged
475 concentration for late arrivals, the adaptive grids reproducing quite consistently the results given by
476 *G*6. The two adaptive strategies also well reproduce the peak concentration given by *G*6. Otherwise,

$G1$ tends to underestimate the largest concentration by approximately 10^{-3} at both locations z_1 and z_2, as depicted in Fig. 8c.

Fig. 9 illustrates comparisons between results obtained with the diverse meshes tested for local values of concentrations C_F and C_S in Eq. (5). Note that, even as the two locations considered are quite close in the domain, the local concentration dynamics exhibit very different characteristics at these points. For example, C_F peaks at $t = 0.1\ t_{PV}$, while C_S attains the largest value at $t = 1.5\ t_{PV}$ and then slowly decreases. The delay observed at these two locations reflects the fact that transport is advection dominated at location P_F, while solute mass exchanges around location P_S are dominated by diffusion and transverse dispersion.

Fig. 9 shows a magnification of C_F at early (Fig. 9b), intermediate (Fig. 9c), and late (Fig. 9d) times for $G6$ (continuous black curves), $G1$ (green curves), $G_{\nabla C}$ (blue curves) and $G_{\nabla CUV}$ (red curves). The differences between $G1$ and $G6$ can reach values up to 10^{-2} and are particularly evident for $t < 0.1\ t_{PV}$, i.e., as long as C_F increases with time (see Fig.s 9b-c). The two adapted meshes are here in close agreement with $G6$. Note that at these early times the two adaptive strategies tend to render later solute arrivals at P_F, while $G1$ yields earlier solute arrivals (due to numerical diffusion). The difference between the solutions given by all the strategies tend to reduce to values below 10^{-4} for $t > 0.1\ t_{PV}$ (Fig.s 9c-d). We observe that the solution associated with $G_{\nabla C}$ displays oscillations of the order of 10^{-5} which are visible at the forward and backward tails. Such oscillations are related to the small inaccuracies noted in Fig. 4 and Fig. 5, and are explained by observing that the local element size at location P_F is characterized by large variations across time.

The temporal variation of concentration C_S (i.e., concentration at point P_S) is depicted in Fig.s 9e-f. Considerable differences appear between $G1$ and $G6$, while the adaptive solutions closely adhere to the results given by the reference solution. For example, one can see that the time of occurrence of a concentration value $C_S = 10^{-5}$ is largely overestimated by $G1$ (see Fig. 9e).

We then consider the evolution of global indicators of spreading and mixing of solute mass in the domain, i.e., S_{zz} in Eq. (7) and χ in Eq. (9). Fig. 10a depicts a comparison between S_{zz} evaluated with $G6$ (black curve), $G1$ (green curve), $G_{\nabla CUV}$ (red curve) and $G_{\nabla C}$ (blue curve). Only limited differences can be noted between the four solutions, $G1$ only slightly overestimating S_{zz} for $t < 0.25$ t_{PV} and otherwise underestimating it. Fig. 10b reveals a marked difference between the scalar dissipation rate χ obtained through $G1$ when compared against reference results obtained through $G6$. Otherwise, $G_{\nabla C}$ and $G_{\nabla CUV}$ provide values of χ which compare extremely well with the reference solution $G6$. This result suggests that, while different meshing strategies may have a reduced impact on the prediction of spreading, they can heavily affect the prediction of mixing, an aspect which can be of relevance also with reference to the simulation of reactive processes.

As a final term of comparison, Fig. 11 depicts the global *a posteriori* error estimator η_C^A (Eq. (12)) for $G6$ (black curve), $G1$ (green curve), $G_{\nabla CUV}$ (red curve) and $G_{\nabla C}$ (blue curve). Note that the value of the estimator provides an approximation of the computational error in the $H1$ seminorm (i.e., based on the gradients of the concentration). Inspection of Fig. 11 reveals that $G1$ shows the highest value of η_C^A across all simulation times. Mesh $G6$ renders the smallest value of η_h^A for $0.05\ t_{PV} < t < t_{PV}$. Note that the slope of the curves for $G_{\nabla C}$ and $G_{\nabla CUV}$ is smaller than that of the curve for $G6$ within the interval $0.05\ t_{PV} < t < t_{PV}$. The smallest slope given by the adaptive procedures within the highlighted temporal interval is consistent with the observation that, even if the spatial gradients in the solution are smearing out, the plume spreads across the z directions. The total plume size increases and the assigned number of elements N_{ele} needs to be cover an area of the domain which increases with time. As a consequence of these dynamics, the reduction in η_C^A is less marked in the adaptive procedure than in $G6$. The elements of the adaptive grid $G_{\nabla C}$ tend to concentrate around the low velocity region at late times, i.e., $t > t_{PV}$ (see Fig. 4). This allows for a proper resolution of concentration gradients which arise around the low velocity region, leading to a sensible reduction of

525 η_C^A (see the marked negative slope of the blue curve in Fig. 11). Interestingly, the values of η_C^A
526 associated with $G_{\nabla C}$ and $G_{\nabla CUV}$ are smaller than those related to *G*6 for $t < 0.05 t_{PV}$, when η_C^A reaches
527 its largest value. Moreover, inspection of meshes $G_{\nabla C}$ and $G_{\nabla CUV}$ at times $t < 0.05\ t_{PV}$ reveals that
528 almost all N_{ele} elements are properly placed near the inlet, with elements having an average size
529 smaller than the one of the uniform elements in *G*6. Therefore, it is reasonable to assume that adaptive
530 grids may lead to a slightly more accurate spatial solution at these early times than the reference *G*6.

531 **4.2 Mildly heterogeneous domain ($\sigma_Y^2 = 1$)**

532 We focus here on the test case with $\sigma_Y^2 = 1$, to assess the sensitivity of the results to the heterogeneity
533 of the porous medium. The *Y* field here considered has been generated with the same seed number
534 used for the case with $\sigma_Y^2 = 5$ to preserve the key features of the spatial structure of the velocity field
535 depicted in Fig. 1b. We omit results related to section-averaged concentrations $\overline{C}_i$, which display a
536 satisfactory agreement between *G*6 and the two adaptive strategies. Fig. 12a depicts the temporal
537 evolution of the local concentrations C_S and C_F for *G*6. We recall that the location of the two points
538 P_F and P_S is not the same as in the highly heterogeneous test case examined in Section 4.1.
539 The overall behaviors of C_S and C_F are not dramatically different, reflecting the reduced influence of
540 the heterogeneity on the concentration, as opposed to the highly heterogeneous setting. Fig. 12b
541 depicts a magnification of C_S at early times. Note the good agreement between the results obtained
542 for *G*6, $G_{\nabla C}$ and $G_{\nabla CUV}$. A good agreement between the results obtained via *G*6, $G_{\nabla C}$ and $G_{\nabla CUV}$ is
543 also evidenced at early time for C_F (not shown) and at late time for both C_F and C_S (see Fig. 12d).
544 The two adaptive strategies well reproduce the observed peak of C_F, as shown in Fig. 12c. A result
545 of similar quality also holds for the peak of C_S (not shown). Results obtained via *G*1 display the
546 smallest peak and heaviest tails, features which can be attributed to the action of numerical dispersion.
547 Fig. 13 depicts the time evolution of (*a*) S_{zz} and (*b*) χ. Similar to the case for $\sigma_Y^2 = 5$, we note that
548 the temporal evolution of S_{zz} and χ associated with $G_{\nabla C}$ and $G_{\nabla CUV}$ is in good agreement with the

549 results obtained through *G*6. Fig.s 13a-b highlight that solute spreading, as represented by S_{zz}, is
550 overestimated and the scalar dissipation rate χ is underestimated for mesh *G*1, a feature which is
551 related to reduced concentration gradients. The adaptive mesh $G_{\nabla CUV}$ provides the smallest S_{zz} and
552 the highest χ values. This is in agreement with the observed general tendency of providing a more
553 compact and sharp evolution of the injected plume by using this adaptive strategy.

554 **5 Conclusions**

555 We apply a space-time adaptive methodology guided by *a posteriori* error estimator for
556 solving solute transport in porous media with spatial distributions of log conductivity *Y* characterized
557 by mild and high levels of heterogeneity. We quantify heterogeneity in terms of the variance, σ_Y^2, of
558 *Y*, which we set to σ_Y^2 = 1 or 5 in our examples. The heterogeneous conductivity fields are
559 synthetically generated on a uniform grid (termed *G*1). We consider nonreactive transport of
560 dissolved chemicals to be governed by an Advection Dispersion Equation at the continuum scale.
561 The key goal of our work is to test the applicability of an automatic mesh and time step adaptation
562 procedure to solve solute transport in such conditions. We implement two strategies to guide the space
563 adaptive procedure. In the first strategy, labeled as $G_{\nabla C}$, the mesh is adapted solely on the basis of
564 the spatial gradients of the concentration field. The second strategy, labeled as $G_{\nabla CUV}$, embeds the
565 spatial gradients of both concentration and velocity components to guide the error estimator. We
566 perform a series of numerical tests and compare the results of the implemented adaptive strategies
567 against those obtained through fixed uniform discretizations. The number of elements of the adapted
568 meshes is kept constant in time and is approximately equal to the number of elements employed in
569 *G*1. The time step is allowed to change within a given range of values (Δt_{MIN}, Δt_{MAX}). The fixed
570 uniform discretization strategies are set such that the spatial meshes are structured and tailored to the
571 spatial structure of *Y* and the time step is fixed to Δt_{MIN}. Our results lead to the following major
572 conclusions:

1. For the highest level of heterogeneity considered ($\sigma_Y^2 = 5$), convergence of the numerical results, as quantified by local and spatially-averaged quantities, is achieved for a numerical uniform grid (*G*6) whose element size is six times smaller than element of *G1*. This result indicates that, in general, it may not be appropriate to routinely employ the same spatial discretization to describe the random conductivity field and numerically approximate solute mass transport. The results associated with grid *G*6 are then taken as a reference against which we test our grid adaptation strategies.
2. Comparison of the results obtained by solving the transport problem on *G*1 against those resulting from the mesh adaptation strategy indicates that only mild differences can be observed when section-averaged concentration and global solute spreading indicators are considered. Otherwise, the use of an appropriate discretization strategy is markedly relevant when local concentration values and global mixing are of concern. This result suggests that mesh adaptation techniques may be well suited to simulation of reactive transport processes.
3. Both adaptive strategies, $G_{\nabla C}$ and $G_{\nabla CUV}$, can reproduce the results obtained through *G*6 in terms of section-averaged and local concentration values, as well as global spreading and mixing metrics. This result is achieved upon reducing the computational cost by approximately one order of magnitude.
4. The two adaptive strategies lead to different meshing of the computational domain along time. Embedding information on both velocity and concentration in the mesh adaptation strategy yields to a more uniform distribution of mesh elements where solute mass is not negligible. However, the two strategies analyzed yield similar results with reference to (section-averaged) concentration breakthrough curves, global mixing and spreading indicators. A key difference is that local concentration values obtained through $G_{\nabla C}$ exhibit oscillations at locations characterized by low concentration gradients and relatively coarse elements. This highlights

597 the importance of controlling the largest element size in the adaptive procedure, when such
598 low values of concentration are of interest.
599 5. The space-time evolution of the $G_{\nabla C}$ and $G_{\nabla CUV}$ meshes suggests that the former is more
600 appropriate to grasp the main features of solute transport taking place within low velocity
601 regions, where diffusion-dispersion mechanisms are dominant, while the latter yields an
602 improved characterization of the forward fringe of solute fronts which propagate through high
603 velocity regions.
604

References

Amaziane, B., Bourgeois, M., El Fatini, M., 2014. Adaptive mesh refinement for a finite volume method for flow and transport of radionuclides in heterogeneous porous media. Oil & Gas Science and Technology – Rev. IFP Energies nouvelles, 69 (4), 687-699.

Berkowitz, B., Cortis, A., Dentz, M., Scher, H., 2006. Modeling non-Fickian transport in geological formations as a continuous time random walk. Rev. Geophys. 44:RG2003, doi:10.1029/2005RG000178.

Bijeljic, B., Blunt, M. J., 2006. Pore-scale modeling and continuous time random walk analysis of dispersion in porous media. Water Resour. Res. 42, W01202, doi:10.1029/2005WR004578.

Bresciani, E., Davy, P. Dreuzy, J., 2012. A finite volume approach with local adaptation scheme for the simulation of free surface flow in porous media. Int. J. Numer. Anal. Methods Geomech. 36 (13), 1574-1591, doi:10.1002/nag.1065.

Brooks, A.N., Hughes, T.J.R., 1982. Streamline upwind/PetrovGalerkin formulations for convection dominated flows with particular emphasis on the incompressible NavierStokes equations. Comput. Methods Appl. Mech. Engrg. 32 (13), 199–259.

Cao, J., Kitanidis, P. K., 1999. Adaptive-grid simulation of groundwater flow in heterogeneous aquifers. Adv. Water Res., 22 (7), 681-696, http://dx.doi.org/10.1016/S0309-1708(98)00047-5.

Chueh, C. C., Secanell, M., Bangerth, W. Djilali, N., 2010. Multi-level adaptive simulation of transient two-phase flow in heterogeneous porous media. J. Comp. Fluid 39, 1585-1596, http://dx.doi.org/10.1016/j.compfluid.2010.05.011.

Cirpka, O. A., Frind, E. O. , Helming, R., 1999. Streamline-oriented grid generation for transport modelling in two-dimensional domains including wells. Adv. Water Resour. 22 (7), 697-710, http://dx.doi.org/10.1016/S0309-1708(98)00050-5.

Cushman, J.H., Ginn, T.R., 1993. Nonlocal dispersion in media with continuously evolving scales of heterogeneity. Transp Porous Media;13(1), 123-38, doi:10.1007/BF00613273.

Dagan, G., 1989. Flow and transport in porous formations, Springer-Verlag, 1989.

631 de Barros, F. P. J., Dentz, M., 2016. Pictures of blockscale transport: Effective versus ensemble
632 dispersion and its uncertainty. Adv. Water Resour. 91, 11-22,
633 http://dx.doi.org/10.1016/j.advwatres.2016.03.004.
634 De Simoni, M., Carrera, J., Sánchez-Vila, X., Guadagnini, A., 2005. A procedure for the solution of
635 multicomponent reactive transport problems. Water Resour. Res. 41, W11410,
636 doi:10.1029/2005WR004056.
637 Deutsch, C. V., Journel, A. G., 1998. GSLIB: Geostatisitcal Software Library and User's Guide, 2nd
638 Ed. New York, Oxford Univerity Press.
639 Dentz, M., de Barros, F. P. J., 2015. Mixing-scale dependent dispersion for transport in heterogeneous
640 flows. J. Fluid Mech. 777, 178-195, https://doi.org/10.1017/jfm.2015.351.
641 Edery, Y., Guadagnini A., Scher, H., Berkowitz, B., 2014. Origins of anomalous transport in
642 heterogeneous media: Structural and dynamic controls. Water Resour. Res. 50, 1490-1505,
643 doi:10.1002/2013WR015111.
644 Esfandiar, B., Porta, G., Perotto, S., Guadagnini, A., 2014. Anisotropic mesh and time step adaptivity
645 for solute transport modeling in porous media. New Challenges in Grid Generation and Adaptivity
646 for Scientific Computing, edited by L. Formaggia and S. Perotto, SEMA SIMAI Springer Series, vol.
647 5, Springer Milan.
648 Esfandiar, B., Porta, G., Perotto, S., Guadagnini, A., 2015. Impact of space-time mesh adaptation on
649 solute transport modeling in porous media. Water Resour. Res. 51, 1315-1332,
650 doi:10.1002/2014WR016569.
651 Formaggia, L., Perotto, S., 2001. New anisotropic a priori error estimates. Numer. Math. 89(4), 641-
652 667, doi:10.1007/s002110100273.
653 Formaggia, L., Perotto, S., 2003. Anisotropic error estimates for elliptic problems. Numer. Math.
654 94(1), 67-92, doi:10.1007/s00211-002-0415-z.

Gedeon, M., Mallants, D., 2012. Sensitivity analysis of a combined groundwater flow and solute transport model using local-grid refinement: A case study. Math. Geosci. 44 (7), 881-899, doi:10.1007/s11004-012-9416-3.

Guadagnini, A., Neuman, S.P., 2001. Recursive conditional moment equations for advective transport in randomly heterogeneous velocity fields, Transport in Porous Media, 42(1/2), 37-67, doi: 10.1023/A:1006791809883.

Haggerty, R., Harvey, C. F., Freiherr von Schwerin, C., Meigs, L. C., 2004. What controls the apparent timescale of solute mass transfer in aquifers and soils? A comparison of experimental results. Water Resour. Res. 40, W01510, doi:10.1029/2002WR001716.

Huang, W., Zhan, X., 2005. Adaptive moving mesh modeling for two dimensional groundwater flow and transport. AMS Contemporary Mathematics, vol. 383, pp. 239–252, Am. Math. Soc., Providence, R. I.

Hecht, F., 2012. New development in FreeFem++. J. Numer. Math. 20 (3-4), 251-265.

Jayasinghe, Y. S., 2015. A space-time adaptive method for flows in oil reservoirs. PhD Theses, Boston.

Kavetski, D., Binning, P., Sloan, S. W., 2002. Adaptive backward Euler time stepping with truncation error control for numerical modelling of unsaturated fluid flow. Int. J. Numer. Methods Eng. 53 (6), 1301-1322, doi:10.1002/nme.329.

Klieber, W., Rivière, B., 2006. Adaptive simulations of two-phase flow by discontinuous Galerkin methods. Comput. Methods Appl. Mech. Engrg. 196, 404-419, http://dx.doi.org/10.1016/j.cma.2006.05.007.

Knupp, P., 1996. A moving mesh algorithm for 3-d regional groundwater flow with water table and seepage face. Adv. Water Res., 19(2), 83-95, http://dx.doi.org/10.1016/0309-1708(95)00033-X.

Le Borgne, T., Dentz, M., Villermaux, E., 2015. The lamellar description of mixing in porous media. J. Fluid Mech. 770, 458-498, doi:https://doi.org/10.1017/jfm.2015.117.

680 Lawrence, A., Rubin, Y., 2007. Block-effective macrodispersion for numerical simulations of sorbing
681 solute transport in heterogeneous porous formations. Adv. Water Resour. 30, 1272- 1285,
682 http://dx.doi.org/10.1016/j.advwatres.2006.11.005.
683 Mansell, R., Ma, L., Ahuja, L., Bloom, S., 2002. Adaptive grid refinement in numerical models for
684 water flow and chemical transport in soil. Vadose Zone J. 1(2), 222-238, doi:10.2113/1.2.222.
685 Mehl, S., Hill, M. C., 2002. Development and evaluation of a local grid refinement method for block-
686 centered finite-difference groundwater models using shared nodes. Adv. Water Resour. 25 (5), 497-
687 511, http://dx.doi.org/10.1016/S0309-1708(02)00021-0.
688 Micheletti, S., Perotto, S., Farrell, P., 2010. A recovery-based error estimator for anisotropic mesh
689 adaptation in CFD. SeMA J. 50(1), 115-137, doi: 10.1007/BF03322545.
690 Morales Casique, E., Neuman, S.P., Guadagnini, A., 2006a. Nonlocal and localized analyses of
691 nonreactive solute transport in bounded randomly heterogeneous porous media: Computational
692 Analysis, Adv. Water Resour., 29, 8, 1399-1418, doi:10.1016/j.advwatres.2005.10.014.
693 Morales-Casique, E., Neuman, S.P., Guadagnini, A., 2006b. Non-local and localized analyses of non-
694 reactive solute transport in bounded randomly heterogeneous porous media: Theoretical framework,
695 Adv. Water Resour. 29, 8, 1238-1255, doi: 10.1016/j.advwatres.2005.10.002.
696 Neuman, S. P., Tartakovsky, D. M., 2009. Perspective on theories of non-Fickian transport in
697 heterogeneous media. Adv. Water Resour. 32, 670-680, doi:10.1016/j.advwatres.2008.08.005.
698 Pepper, D., Stephenson, D., 1995. An adaptive finite-element model for calculating subsurface
699 transport of contaminant. Ground Water, 33 (3), 486-496, doi:10.1111/j.1745-6584.1995.tb00305.x.
700 Porta, G., Perotto, S., Ballio, F., 2012a. Anisotropic mesh adaptation driven by a recovery-based error
701 estimator for shallow water flow modeling. Int. J. Numer. Methods Fluids 70(3), 269-299,
702 doi:10.1002/fld.2688.
703 Porta, G., Perotto, S., Ballio, F., 2012b. A space-time adaptation scheme for unsteady shallow water
704 problems. Math. Comput. Simul., 82(12), 2929-2950, doi:10.1016/j.matcom.2011.06.004
705 Quarteroni, A., Sacco, R., Saleri, F., 2007. Numerical Mathematics vol. 37, Springer, Berlin.

706 Riva, M., Guadagnini, A., Fernandez-Garcia, D., Sanchez-Vila, X., Ptak, T., 2008. Relative
707 importance of geostatistical and transport models in describing heavily tailed breakthrough curves at
708 the Lauswiesen site. J. Contam. Hydrol. 101, 1-13, doi:10.1016/j.jconhyd.2008.07.004.
709 Riva M., Guadagnini, L., Guadagnini, A., 2010. Effect of uncertainty of lithofacies, conductivity an
710 porosity distributions on stochastic interpretations of a field scale tracer test, Stochastic
711 Environmental Research and Risk Assessment, 24, 955-970, doi:10.1007/s00477-010-0399-7.
712 Saaltink, M. W., Carrera, J., Olivella, S., 2004. Mass balance errors when solving the convective form
713 of the transport equation in transient flow problems. Water Resour. Res. 40, W05107,
714 doi:10.1029/2003WR002866.
715 Salles, J., Thovert, J.-F., Delannay, R., Prevors, L., Auriault, J.-L., Adler, P. M., 1993. Taylor
716 dispersion in porous media: Determination of the dispersion tensor. Phys. Fluids A 5, 2348-2376,
717 doi:http://dx.doi.org/10.1063/1.858751.
718 Taylor, G. I., 1953. Dispersion of soluble matter in solvent flowing slowly through a tube. Proc. Royal
719 Soc. London, 219(1137):186-203, doi:10.1098/rspa.1953.0139
720 Younes, A., Ackerer, P., 2010. Empirical versus time stepping with embedded error control for
721 density-driven flow in porous media. Water Resour. Res. 46, W08523, doi:10.1029/2009WR008229.
722 Zhang, Y., Benson, D. A., Meerschaert, M. M., LaBolle, E. M., 2007. Space-fractional advection–
723 dispersion equations with variable parameters: diverse formulas, numerical solutions, and application
724 to the macrodispersion experiment site data. Water Resour. Res. 43:W05439,
725 doi:10.1029/2006WR004912.
726 Zienkiewicz, O. C. and Zhu, J. Z., 1987. A simple error estimator and adaptive procedure for practical
727 engineering analysis. Int. J. Numer. Methods Eng. 24 (2), 337-357, doi:10.1002/nme.1620240206.
728
729
730
731
732

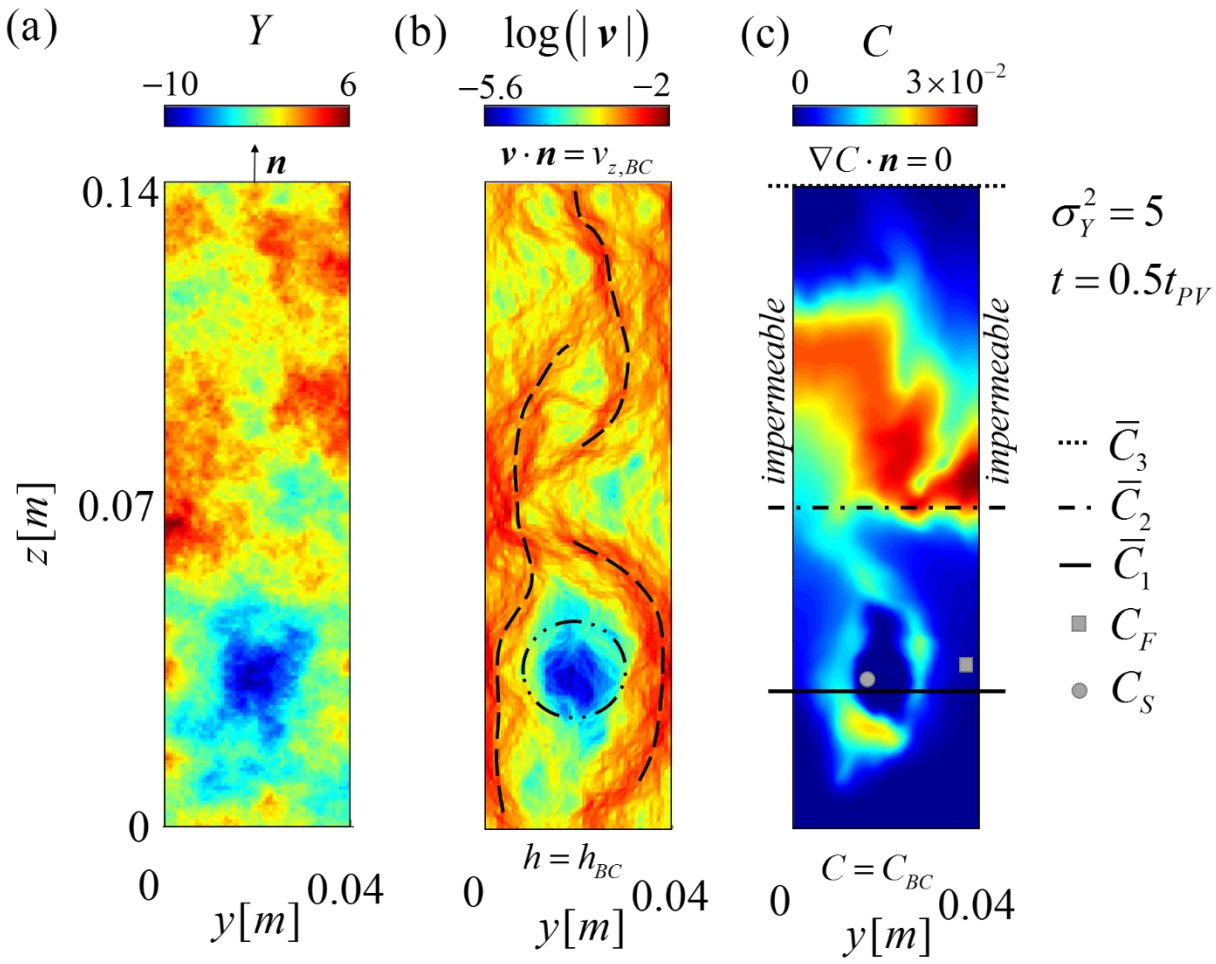

Fig. 1. Test case with $\sigma_Y^2 = 5$: (a) Spatial distribution of the log-conductivity field *Y*, (b) spatial distribution of the (natural) logarithm of the velocity modulus, (c) solute concentration field at $t = 0.5\ t_{PV}$. High-velocity channels (dashed lines) and the low velocity region (dash-dotted line) are highlighted in (b). Locations associated with section averaged concentrations $\bar{C}_1$, $\bar{C}_2$, $\bar{C}_3$ and local concentrations C_F, C_S are identified in (c) (see text for definitions). Imposed boundary conditions for the flow and transport problems are respectively included in panels (b) and (c).

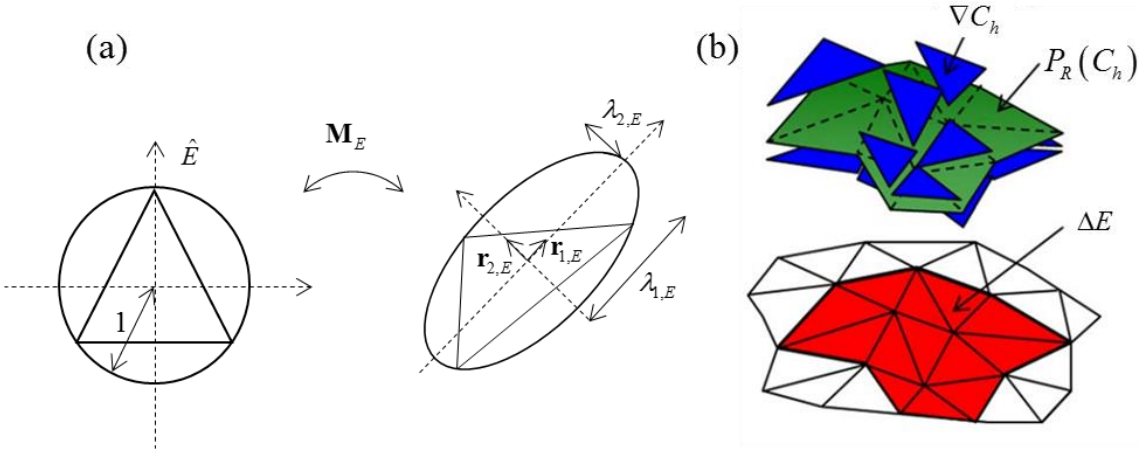

742

743

744 Fig. 2. Spatial error estimator $\eta^A_{E,C}(t)$ in (11): definition sketch of (a) the anisotropic setting, and (b)

745 the recovered gradient $P_R(C_h)$.

746

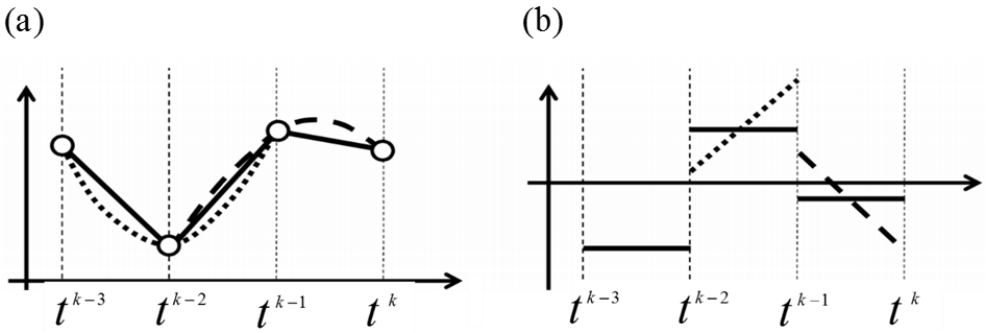

747

748 Fig. 3. Time derivative recovery procedure: (a) recovered solution C_R (dotted and dashed lines) versus

749 linear interpolant of values C_h (continuous line) and (b) comparison between the time derivatives

750 $\partial C_R / \partial t$ (dotted and dashed lines) and $\partial C_h / \partial t$ (continuous lines)

751

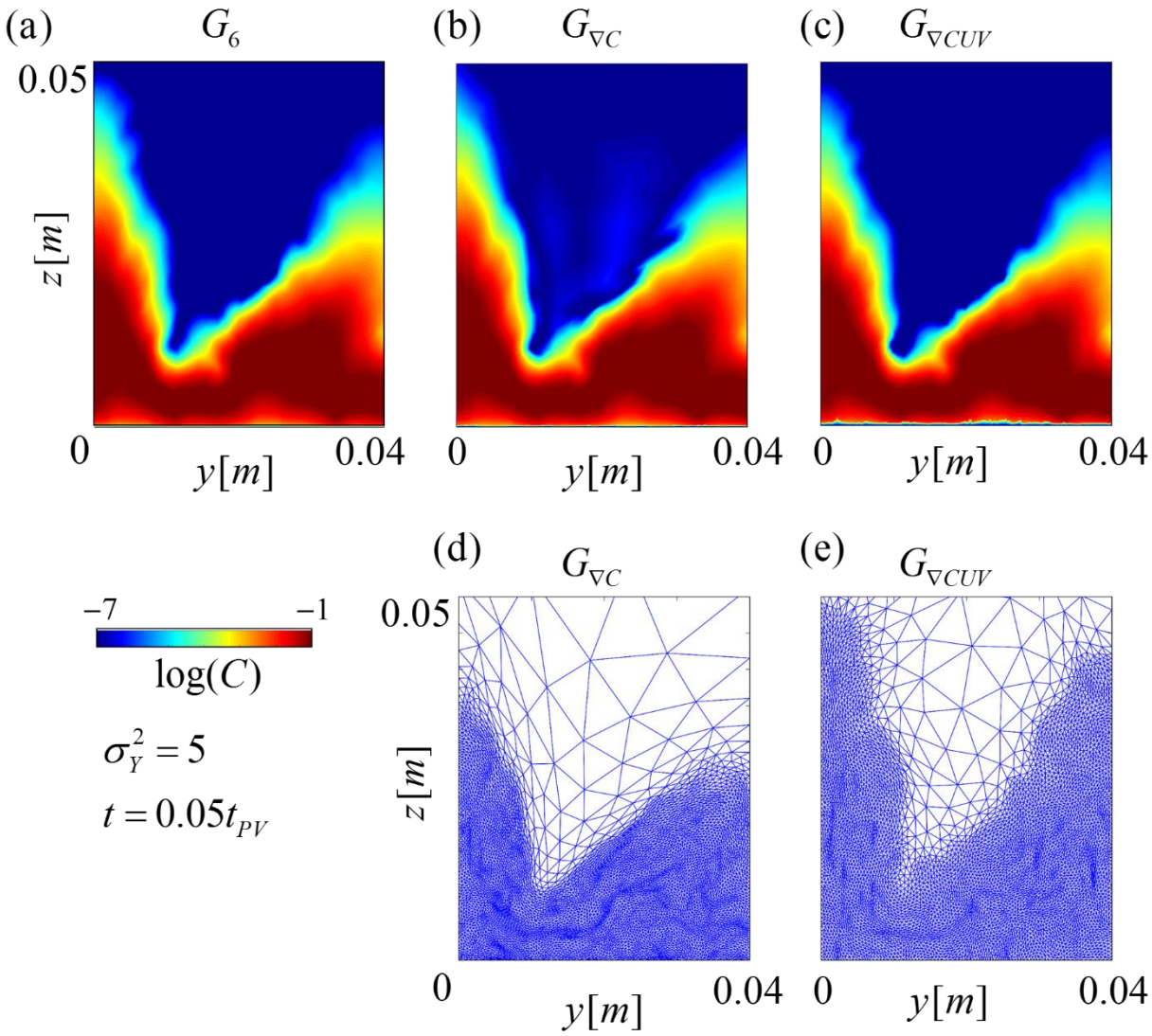

752

753

754 Fig. 4. Test case with $\sigma_Y^2 = 5$: spatial distribution of the concentration field (in logarithmic scale)

755 within a subset of the domain close to inlet at time $t = 0.05t_{PV}$, for discretization (a) $G6$; (b) $G_{\nabla C}$; (c)

756 $G_{\nabla CUV}$ and the associated adapted meshes for (d) $G_{\nabla C}$; (e) $G_{\nabla CUV}$.

757

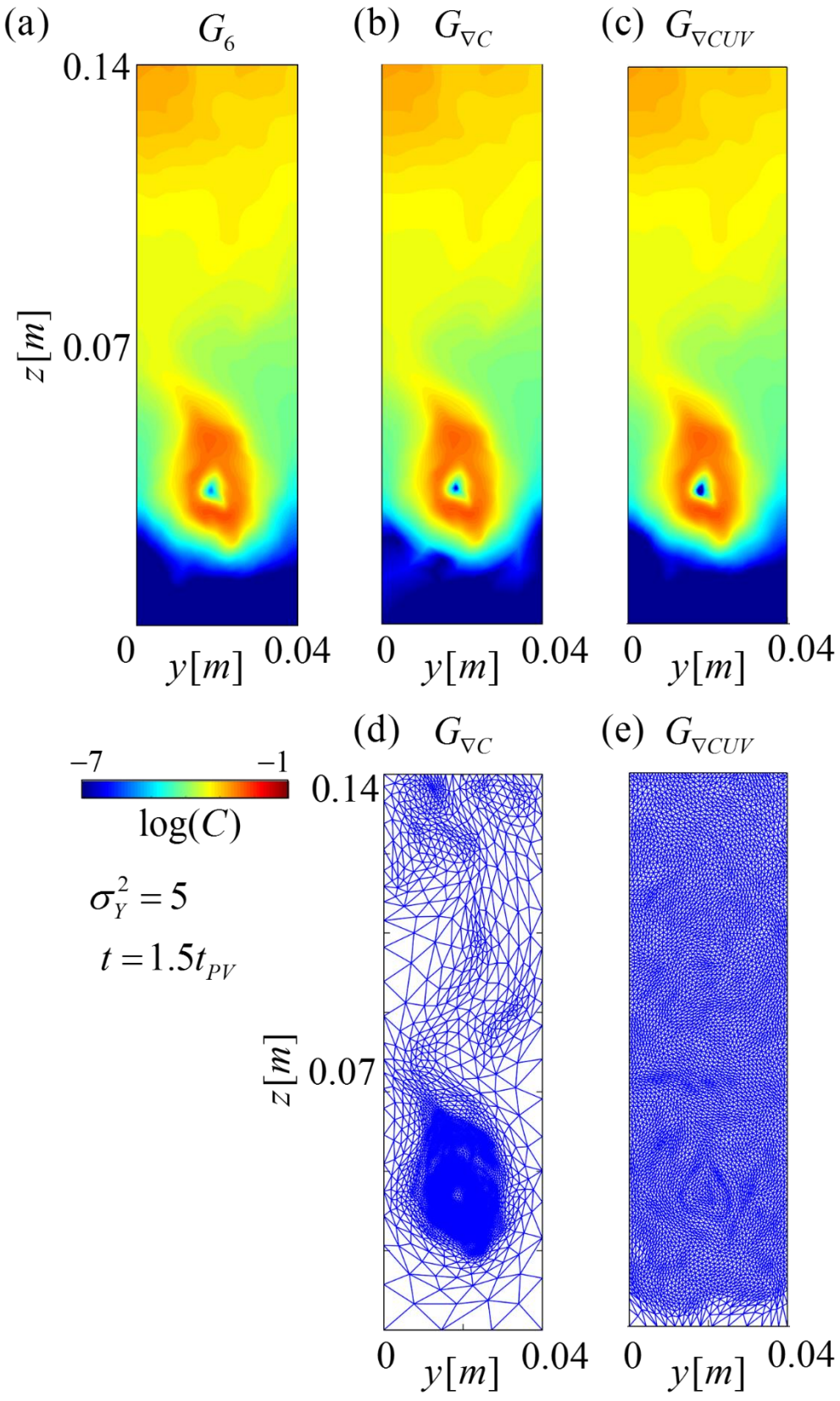

758

759 Fig. 5. Test case with $\sigma_Y^2 = 5$: spatial distribution of the concentration field (in logarithmic scale)

760 within the simulation domain at time $t = 1.5t_{PV}$, for discretization (a) $G6$; (b) $G_{\nabla C}$; (c) $G_{\nabla CUV}$ together

761 with the associated adapted meshes for (d) $G_{\nabla C}$; (e) $G_{\nabla CUV}$.

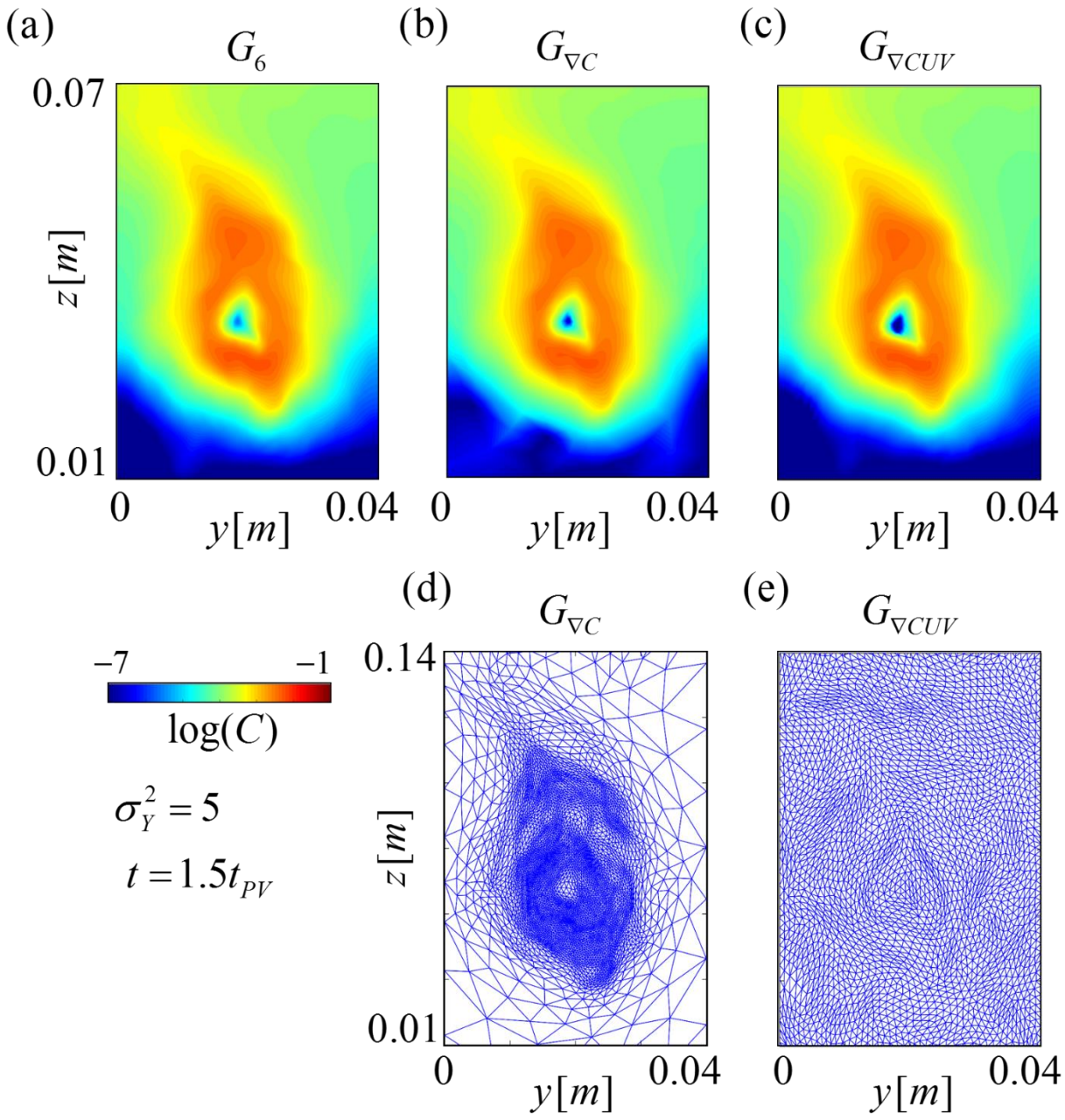

762

763

764 Fig. 6. Test case with $\sigma_Y^2 = 5$: spatial distribution of the concentration field (in logarithmic scale) in

765 the low velocity region evidenced in Fig. 1b for t = 1.5t_{PV} and discretization (a) $G6$; (b) $G_{\nabla C}$; (c)

766 $G_{\nabla CUV}$ together with the associated adapted meshes for (d) $G_{\nabla C}$; (e) $G_{\nabla CUV}$.

767

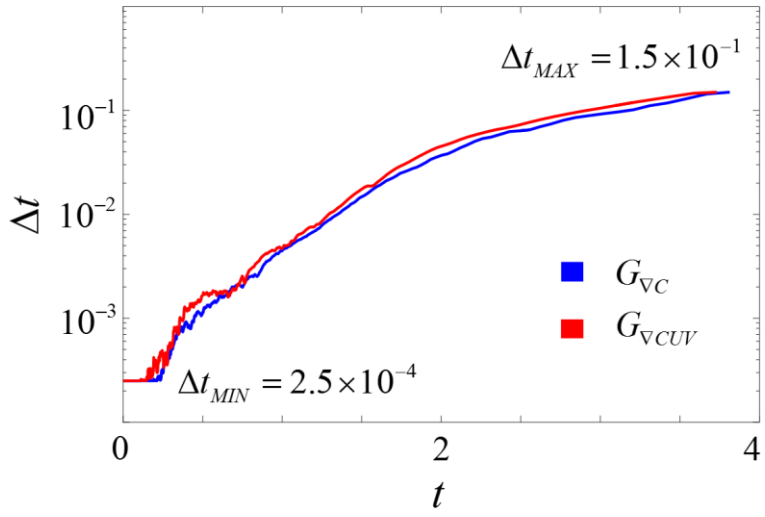

768

769 Fig. 7. Test case with $\sigma_Y^2 = 5$: temporal evolution of the adaptive time step, Δt.

770

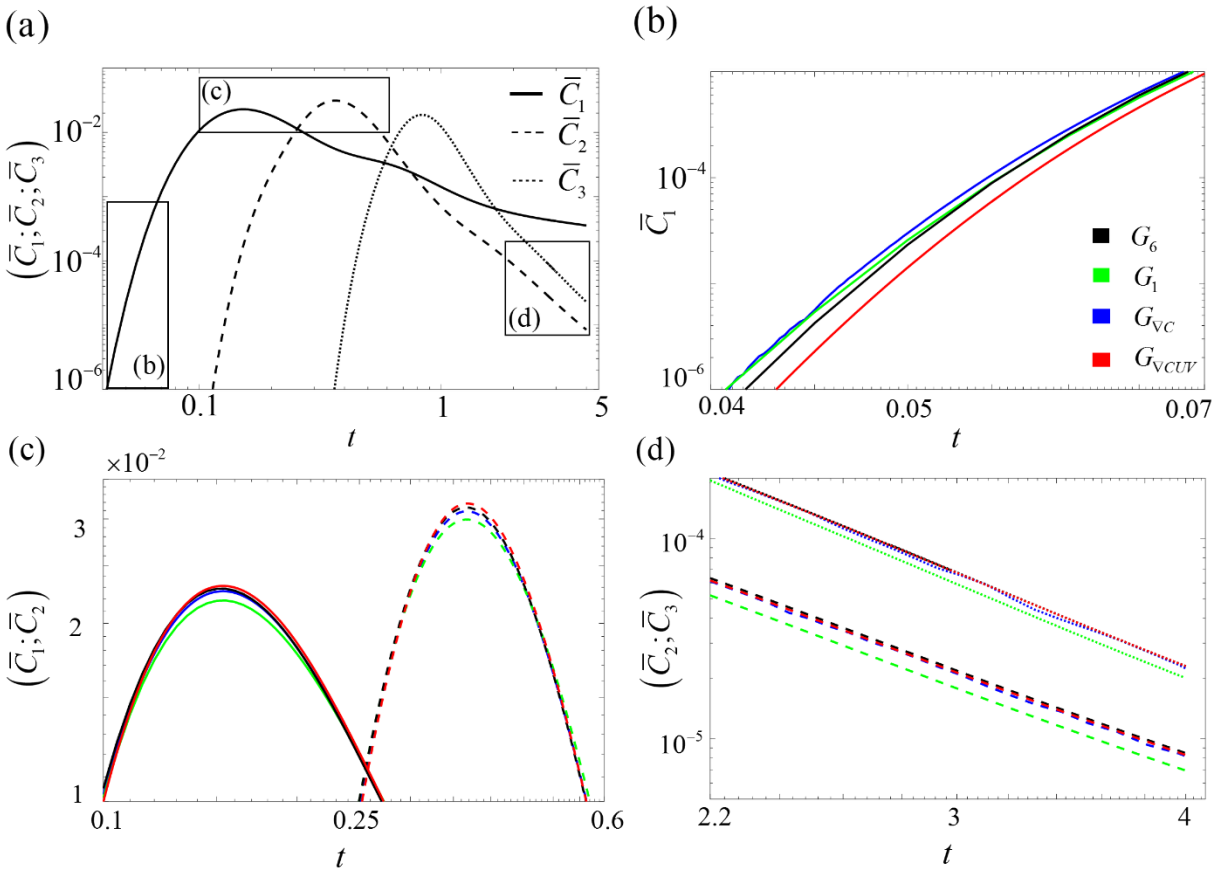

771

772 Fig. 8. Test case with $\sigma_Y^2 = 5$: temporal evolution of the section-averaged concentrations $\bar{C}_1$
773 (continuous curves), $\bar{C}_2$ (dashed curves), and $\bar{C}_3$ (dotted curves), for (a) $G6$. Panels (b-d) display the
774 comparisons between solutions given by $G1$, $G6$, $G_{\nabla C}$, $G_{\nabla CUV}$, associated with early times (b), peak
775 (c) and late times (d), as indicated in panel (a).

776

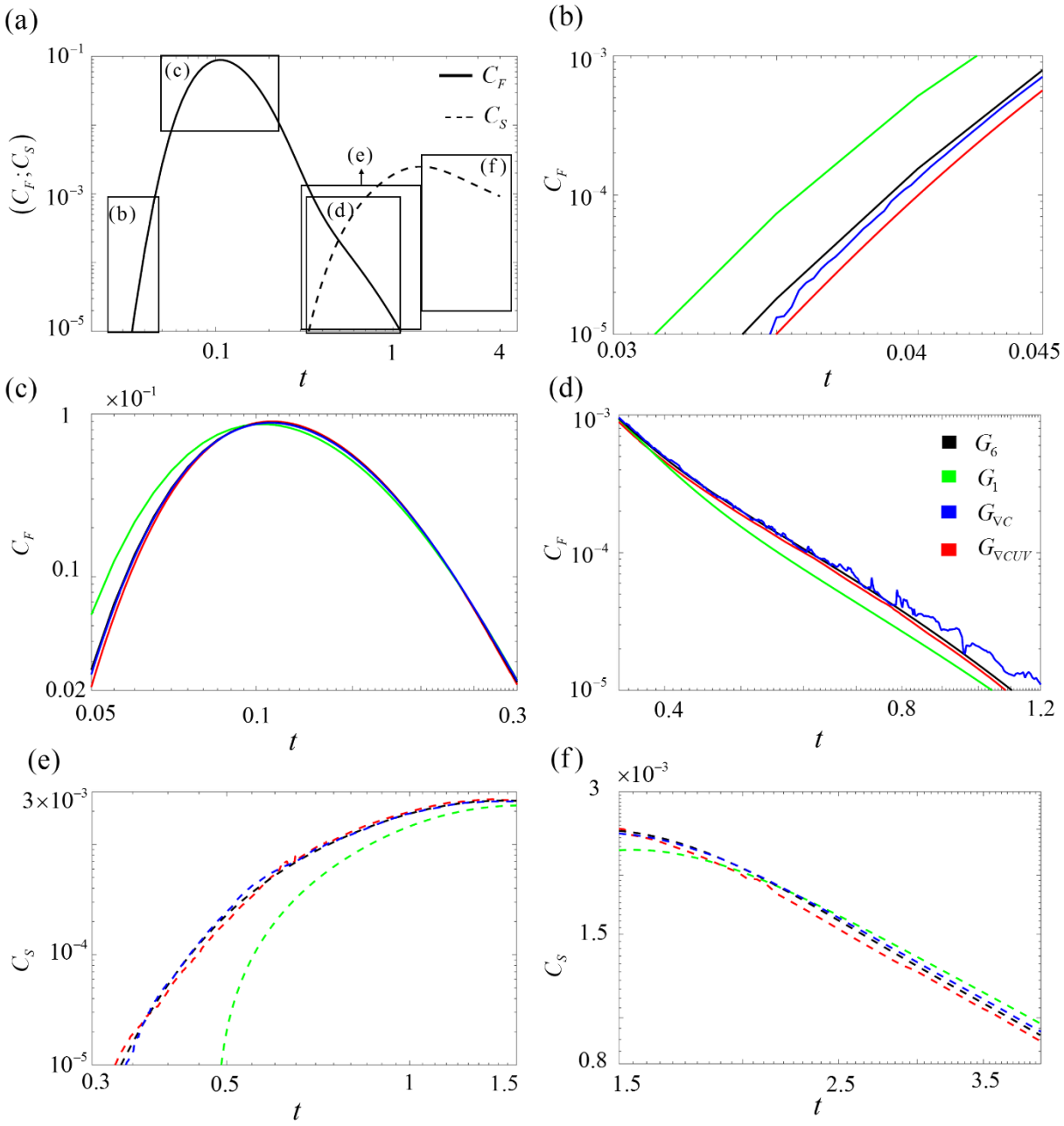

Fig. 9. Test case with $\sigma_Y^2 = 5$: temporal evolution of the local concentration values C_F (continuous curves) and C_S (dashed curves), for (a) $G6$. Panels (b-f) display the comparisons between solutions given by $G1$, $G6$, $G_{\nabla C}$, $G_{\nabla CUV}$ related to specific time intervals for C_F (b-d) and C_S (e-f) as indicated in panel (a).

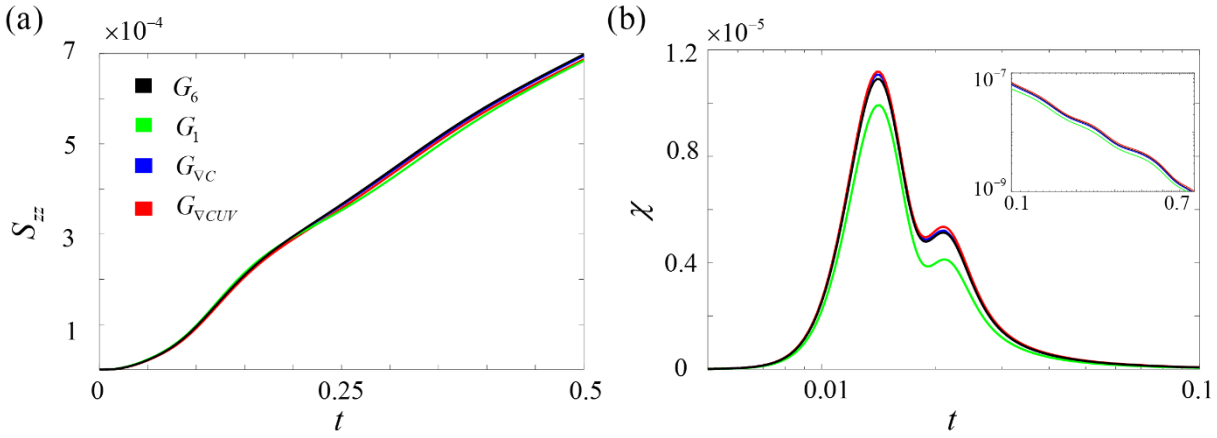

783

784 Fig. 10. Test case with $\sigma_Y^2 = 5$: time evolution of (a) solute plume spreading, S_{zz}, and (b) scalar

785 dissipation rate, χ .

786

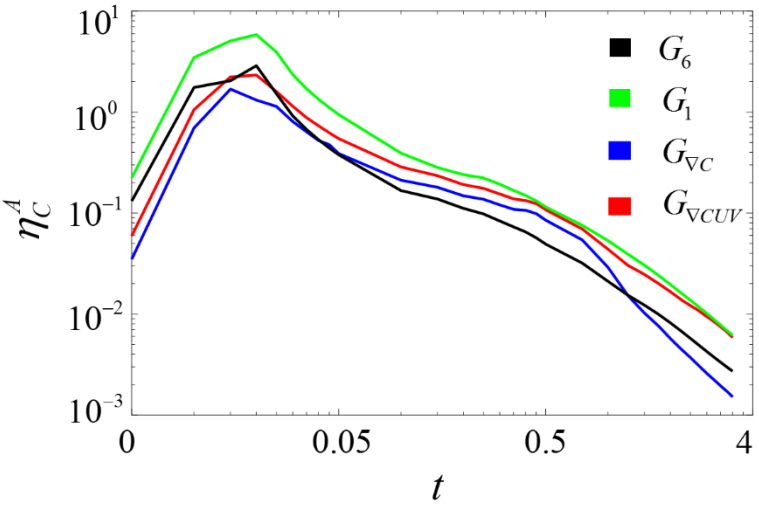

787

788 Fig. 11. Test case with $\sigma_Y^2 = 5$: Time evolution of the *a posteriori* estimator $\eta_C^A(t)$ in Eq. (12).

789

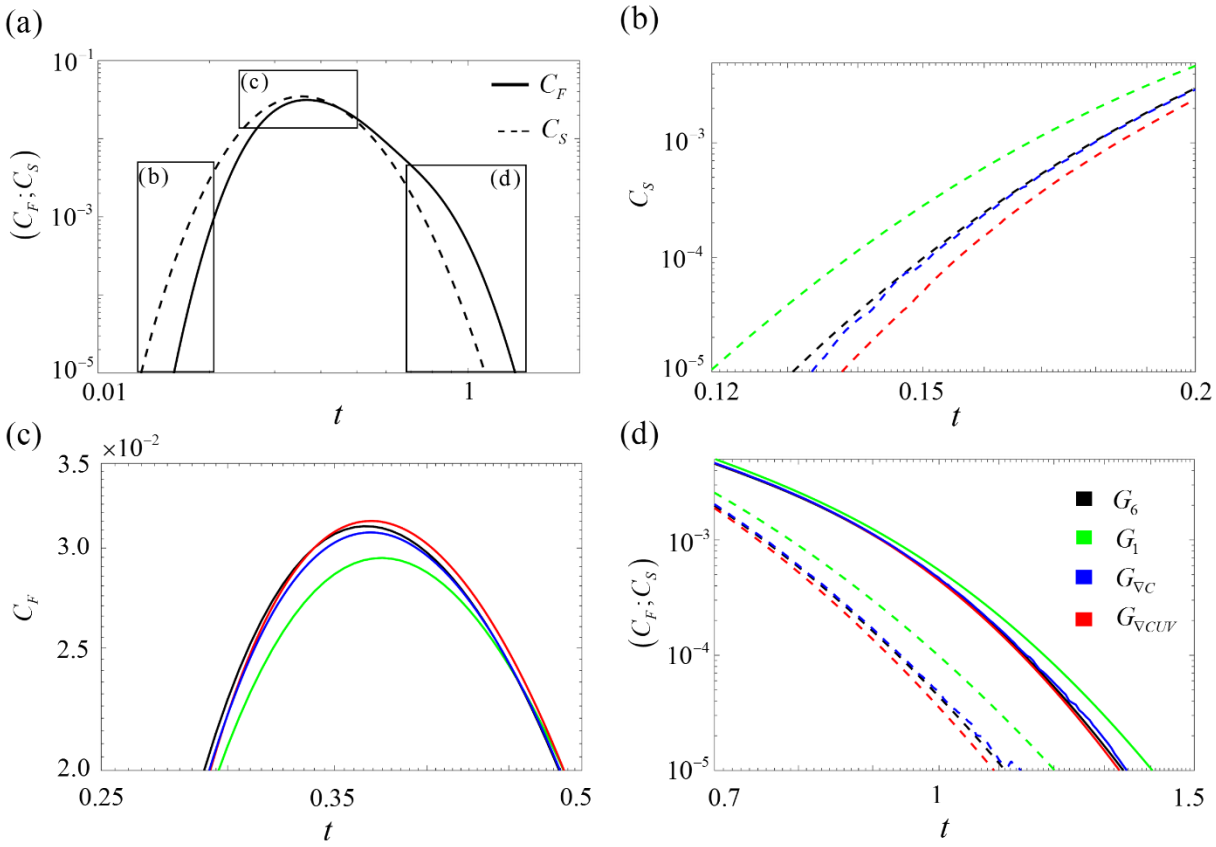

Fig. 12. Test case with $\sigma_Y^2 = 1$: time evolution of the local concentration values C_F (continuous curves) and C_S (dashed curves), for (a) $G6$. Panels (b-d) display the comparisons between solutions given by $G1$, $G6$, $G_{\nabla C}$, $G_{\nabla CUV}$ and related to specific time intervals for C_F (c-d) and C_S (b,d), as indicated in panel (a).

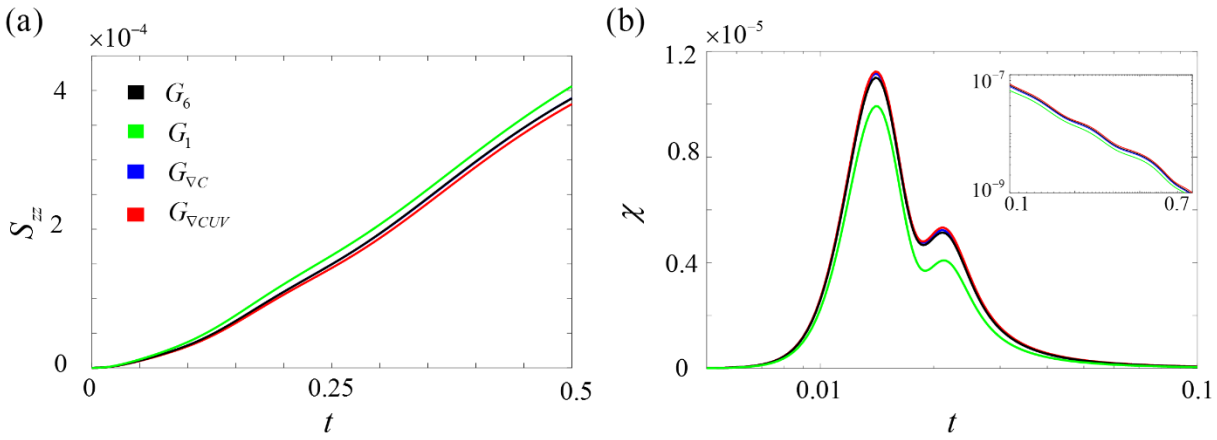

796

797 Fig. 13. Test case with $\sigma_Y^2 = 1$: temporal evolution of (a) solute plume spreading, S_{zz}, and (b) scalar

798 dissipation rate, χ.

799

800